

**Surpassing the Theoretical Limit of Porosity in Conventional
Solid-State Foaming: Microstructure Characterization of
Length Scales in a Copper Metal Foam**

by Mark A Tschopp, Kris A Darling, Mark A Atwater

ARL-TR-7139

November 2014

NOTICES

Disclaimers

The findings in this report are not to be construed as an official Department of the Army position unless so designated by other authorized documents.

Citation of manufacturer's or trade names does not constitute an official endorsement or approval of the use thereof.

Destroy this report when it is no longer needed. Do not return it to the originator.

Army Research Laboratory

Aberdeen Proving Ground, MD 21005-5069

ARL-TR-7139

November 2014

Surpassing the Theoretical Limit of Porosity in Conventional Solid-State Foaming: Microstructure Characterization of Length Scales in a Copper Metal Foam

Mark A Tschopp and Kris A Darling
Weapons and Materials Research Directorate, ARL

Mark A Atwater
Department of Applied Engineering, Safety & Technology
Millersville University

REPORT DOCUMENTATION PAGE				<i>Form Approved</i> OMB No. 0704-0188	
Public reporting burden for this collection of information is estimated to average 1 hour per response, including the time for reviewing instructions, searching existing data sources, gathering and maintaining the data needed, and completing and reviewing the collection information. Send comments regarding this burden estimate or any other aspect of this collection of information, including suggestions for reducing the burden, to Department of Defense, Washington Headquarters Services, Directorate for Information Operations and Reports (0704-0188), 1215 Jefferson Davis Highway, Suite 1204, Arlington, VA 22202-4302. Respondents should be aware that notwithstanding any other provision of law, no person shall be subject to any penalty for failing to comply with a collection of information if it does not display a currently valid OMB control number. PLEASE DO NOT RETURN YOUR FORM TO THE ABOVE ADDRESS.					
1. REPORT DATE (DD-MM-YYYY) November 2014		2. REPORT TYPE Final		3. DATES COVERED (From - To) November 2012–November 2014	
4. TITLE AND SUBTITLE Surpassing the Theoretical Limit of Porosity in Conventional Solid-State Foaming: Microstructure Characterization of Length Scales in a Copper Metal Foam				5a. CONTRACT NUMBER	
				5b. GRANT NUMBER	
				5c. PROGRAM ELEMENT NUMBER	
6. AUTHOR(S) Mark A Tschopp, Kris A Darling, and Mark A Atwater				5d. PROJECT NUMBER	
				5e. TASK NUMBER	
				5f. WORK UNIT NUMBER	
7. PERFORMING ORGANIZATION NAME(S) AND ADDRESS(ES) US Army Research Laboratory ATTN: RDRL-WMM-F Aberdeen Proving Ground, MD 21005-5069				8. PERFORMING ORGANIZATION REPORT NUMBER ARL-TR-7139	
9. SPONSORING/MONITORING AGENCY NAME(S) AND ADDRESS(ES)				10. SPONSOR/MONITOR'S ACRONYM(S)	
				11. SPONSOR/MONITOR'S REPORT NUMBER(S)	
12. DISTRIBUTION/AVAILABILITY STATEMENT Approved for public release; distribution is unlimited.					
13. SUPPLEMENTARY NOTES					
14. ABSTRACT Solid-state processes for creating metal foams are often complex and/or time consuming, and in methods such as gas entrapment, there are practical limits to the porosity achievable due to pore coalescence and percolation. A simple process has been developed to create copper-based metal foam with porosity greater than 65%. The process is unique as expansion occurs within particles, not between them. The method is applied to create a bulk part. The microstructure length scales of the foamed particles are examined using 1- and 2-point microstructure statistics.					
15. SUBJECT TERMS characterization; solid-state foaming; nanostructured metal foam; copper; microstructure; porosity; correlation functions					
16. SECURITY CLASSIFICATION OF:			17. LIMITATION OF ABSTRACT UU	18. NUMBER OF PAGES 60	19a. NAME OF RESPONSIBLE PERSON Mark A Tschopp
a. REPORT Unclassified	b. ABSTRACT Unclassified	c. THIS PAGE Unclassified			19b. TELEPHONE NUMBER (Include area code) 410-306-0855

Contents

List of Figures	v
Acknowledgments	viii
1. Introduction	1
2. Solid-State Foaming Technique	2
2.1 Experimental Methodology	2
2.2 Foam Microstructure Characterization.....	8
2.3 Foaming Mechanism.....	9
2.4 Part Production	9
3. Digital Image Processing	11
3.1 Imaging Porosity in Foamed Powder Particles	11
3.2 3-D Reconstruction Method for Foamed Powder Microstructure	13
4. Microstructure Characterization	19
4.1 Two-Point Correlation Function Definition.....	19
4.2 Lineal Path Function Definition	20
4.3 One-Point and Two-Point Statistics of Foamed Powder Particles	22
4.3.1 One-Point Statistics	22
4.3.2 Two-Point Correlation Function Statistics	23
4.3.3 Lineal Path Function Statistics	32

5. Conclusions	34
6. References	35
Appendix A. MATLAB TPCF Nonperiodic Function	39
Appendix B. MATLAB TPCF Periodic Function	43
Appendix C. MATLAB LPF Nonperiodic Function	45
List of Symbols, Abbreviations, and Acronyms	49
Distribution List	50

List of Figures

Fig. 1 SEM imaging of powder particles shows the following features: a) loose powder morphology, b) cross section of large powder particle showing porosity extends through the bulk, c) cross section through the center of a powder particle, and d) the corresponding FIBCCI image.....	3
Fig. 2 SEM imaging of powder particles shows porosity intersecting with the surface of the powder. The inset image shows the porosity just below the surface after FIB through a cross section of the particle.	4
Fig. 3 FIBICC imaging of Cu 5% Sb alloy annealed at 600 °C for 1 h: a) low-magnification image of particle cross section showing considerable porosity, b) high-magnification images showing pore structure, and c) image of particle surface consisting of small grains within magnified inset.....	6
Fig. 4 EBSD of foamed particle cross section. Note the random orientation and the confirmation of a fine grain size at free surfaces.	7
Fig. 5 a) 2-D images showing the different stages of analysis necessary to reconstruct the 3-D volume including image capture, image segmentation, binary image, and fused image. b) 3-D volume reconstruction of matrix structure (foreground) and pore structure (background) within a particle.....	8
Fig. 6 The ease of processing allows for complex parts to be created. This “pawn” was made by filling a 2-piece mold with the Cu alloy powder and applying pressure at one end with a machine screw. The detail of the mold was reproduced with significant accuracy (scale in centimeters).....	11
Fig. 7 SEM image of a Cu–Sb foamed particle generated by the solid-state foaming technique	12
Fig. 8 SEM image of a Cu–Sb foamed particle generated by the solid-state foaming technique: a) same powder particle as that in Fig. 7, and b) second powder particle that exhibits the same pore structure	13

Fig. 9 Close-up SEM image of a Cu–Sb foamed particle generated by the solid-state foaming technique. The ability to observe the pore structure below the FIB surface on the SEM image indicates that these pores appear tortuous (nonspherical) and highly interconnected.....	14
Fig. 10 Manual segmentation of SEM image of a Cu–Sb foamed particle generated by the solid-state foaming technique. After manually tracing the pores, the images were scanned and the pore outlines were automatically identified via image processing.	16
Fig. 11 SEM binary image of a Cu–Sb foamed particle where black is the matrix and white is the porosity. This binary image can be used for subsequent characterization of the microstructure statistics.	17
Fig. 12 Segmented SEM image of a Cu–Sb foamed particle where the matrix is green, the pores are blue, and the red lines are the pore boundaries	18
Fig. 13 One-dimensional schematic showing the difference between TPCF $P_{11}(r)$ and LPF $L_{11}(r)$ for distances of $r = \{1, 2, 3\}$	21
Fig. 14 The variation in area fraction as a function of the FIB slices through the 3-D dataset ..	22
Fig. 15 TPCF as a function of distance for $\theta = 0^\circ$ (enlargement of Fig. 16a). The red curves denote the TPCFs from the different slices and the black curve is the mean TPCF throughout the entire 3-D dataset.	23
Fig. 16 TPCF as a function of distance for θ of a) 0° , b) 90° , c) $+45^\circ$, and d) -45° . The red curves denote the TPCFs from the different slices and the black curve is the mean TPCF over the entire 3-D dataset in the various directions.	24
Fig. 17 Normalized TPCF as a function of distance for θ of a) 0° , b) 90° , c) $+45^\circ$, and d) -45° . The red curves denote the TPCFs from the different slices and the black curve is the mean TPCF over the entire 3-D dataset in the various directions.	26
Fig. 18 Normalized TPCF as a function of distance for θ of a) 0° , b) 90° , c) $+45^\circ$, and d) -45° . The dashed lines bounding the mean TPCF represent 1 standard deviation from the mean.	27

- Fig. 19 The mean normalized TPCFs for the 4 directions along with the 1 standard deviation lines. The microstructure approaches $P_{11} = 1$ within $2 \mu\text{m}$. Beyond $2 \mu\text{m}$, the TPCF approaches that given by the area fraction of porosity squared (i.e., f_1^2), i.e., a purely random correlation between porosity. 28
- Fig. 20 The mean normalized TPCFs for the 4 directions along with the representative length scales given by the TPCF intersection with $P_{11} = 1.1$ and $P_{11} = 1.5$ for the porosity29
- Fig. 21 The normalized TPCFs for the matrix phase for the 4 directions for the slices shows similar variability and length scales as the porosity TPCFs (a–d). The mean TPCFs for the matrix in the 4 directions was computed along with the representative length scales given by the TPCF intersection with $P_{22} = 1.1$ and $P_{22} = 1.5$ (e). 31
- Fig. 22 LPF as a function of distance for θ of 0° (a,c); 90° (b,d); for the porosity, i.e., $L_{11}(r, \theta)$ (a,b); and the matrix, i.e., $L_{22}(r, \theta)$ (c,d). The colored lines are the LPF computed from individual slices (red for porosity, blue for matrix) and the dashed lines show the calculation of the length scale for particular values of the LPF. 33

Acknowledgments

The authors also extend their appreciation and acknowledge the contributions of the following individuals in this work: Dr Heather Murdoch, Mr Anthony Roberts, and Mr Jim Catalano. The authors would also like to acknowledge discussions with Dr Tony Fast (Georgia Institute of Technology) pertaining to the use of fast Fourier transforms to calculate 2-point correlation statistics in MATLAB.

1. Introduction

Metallic foams and porous metal structures are valuable for their unique characteristics such as high specific strength, energy absorption at constant crushing load, efficient heat transfer and acoustic properties, all of which can be tailored by controlling the porosity.^{1–3} Many techniques for generating metal foams exist, but the vast majority of metal foam production is through liquid state processes such as the melt processing of aluminum by gas injection or decomposition of a dispersed foaming agent.⁴ Aluminum has dominated the metal foam industry due its low melting temperature and relative stability in air.⁵ More reactive metals and those with higher melting temperatures require special processing, usually through solid-state techniques.^{3,6–11} In the solid-state foaming process,^{12,13} metal foams are typically produced using a 2-step process: 1) entrapping gas within the interparticle voids during powder consolidation and 2) heating to expand the entrapped gas such that the internal pressure exceeds the yield strength and enables plasticity or creep to increase porosity.¹⁴ While some powder metallurgy processes (e.g., using a polymer foam as a fugitive template⁷) can exceed 85% porosity, it is more common for powder metallurgy processes to produce porosity levels between 20% and 40%.^{5,14} In fact, Elzey and Wadley¹⁴ calculated that the limit of the solid-state foaming process by gas entrapment is approximately 65% porosity, even under ideal, superplastic conditions. Experimentally, this method has produced foams with porosity only as high as 53%,¹⁵ but porosity using solid-state foaming has typically been limited to approximately 40%. These relatively low porosity levels (compared to liquid-state processes) constrain the applications of metal foams produced via solid-state foaming.

The current limitation of solid-state expansion is based on gas entrapment between solid particles during consolidation. In this model, the initial gas pressure and foaming temperature determine the resulting porosity. However, if the expanding gas is not limited to just that which is trapped between particles, but is also located within particles, solid-state foaming may assume a character more akin to expandable polymers that foam from the constituent pellets. This concept is a paradigm shift in terms of the solid-state foaming process and the achievable levels of porosity. In this technical report, we examine the microstructure and morphology of a copper–antimony (Cu–Sb) alloy that expands to porosities of close to 40% within individual particles, resulting in absolute porosity of 69% in sintered samples.

2. Solid-State Foaming Technique

2.1 Experimental Methodology

The Cu-Sb alloy powder was formed by mechanically alloying Cu and Sb (Alfa Aesar, 99.9% and 99.5%, respectively) at cryogenic temperature ($-196\text{ }^{\circ}\text{C}$) for 4 h using a modified SPEX 8000M Mixer/Mill. The elemental powders were combined to achieve 5 atomic percent (at%) Sb in Cu. The alloyed powder was annealed at $600\text{ }^{\circ}\text{C}$ for a period of 1 h under 3% H_2 (balance Ar). Microscopic examination of the powders was carried out using an FEI Nova Nano Lab 600 dual beam microscope using scanning electron microscopy (SEM). Cross-sectional analysis was performed using a focused ion beam (FIB). The grain size and grain orientations were measured using focused ion beam channeling contrast imaging (FIBCCI) images and electron backscatter diffraction (EBSD), respectively. FIB serial sectioning of the individual powder particles was used to visualize and quantify a representative 3-dimensional (3-D) pore structure in a volume $25.6\text{-}\mu\text{m}$ wide, $22.1\text{-}\mu\text{m}$ high, and $12.5\text{-}\mu\text{m}$ deep. The as-milled powders were also compacted in a 3-mm die. The compacts were weighed before and after annealing to measure the apparent density.

The annealed Cu-Sb particles were approximately $60\text{ }\mu\text{m}$ in size and irregularly shaped after foaming (Fig. 1). Cross-sectional characterization of these particles revealed that significant expansion had occurred within each particle (Fig. 1). The amount of porosity shows a relatively even distribution throughout each particle, with a mean equivalent pore diameter of $1.02\text{ }\mu\text{m}$ with a standard deviation of $0.89\text{ }\mu\text{m}$ as measured from 2-dimensional (2-D) images (5,588 pores). This is in contrast to the typical pore sizes reported as a result of gas expansion studies, which are approximately $250\text{ }\mu\text{m}$, more than 2 orders of magnitude larger than the pore sizes observed here. At the given temperature and hold time ($600\text{ }^{\circ}\text{C}$, 1 h), the pores are found to be highly interconnected, not only with each other, but with the free surface of their respective particles as well (Fig. 2). A video of the FIB serial sectioning of a single particle¹⁶ shows the continuity of the pore structure caused by extensive void coalescence. Interestingly, there is no straight path for porosity to connect surfaces even in small particles. Rather, the porosity forms a tortuous passage from surface to surface, which is not entirely obvious without reconstructing the 3-D pore structure.

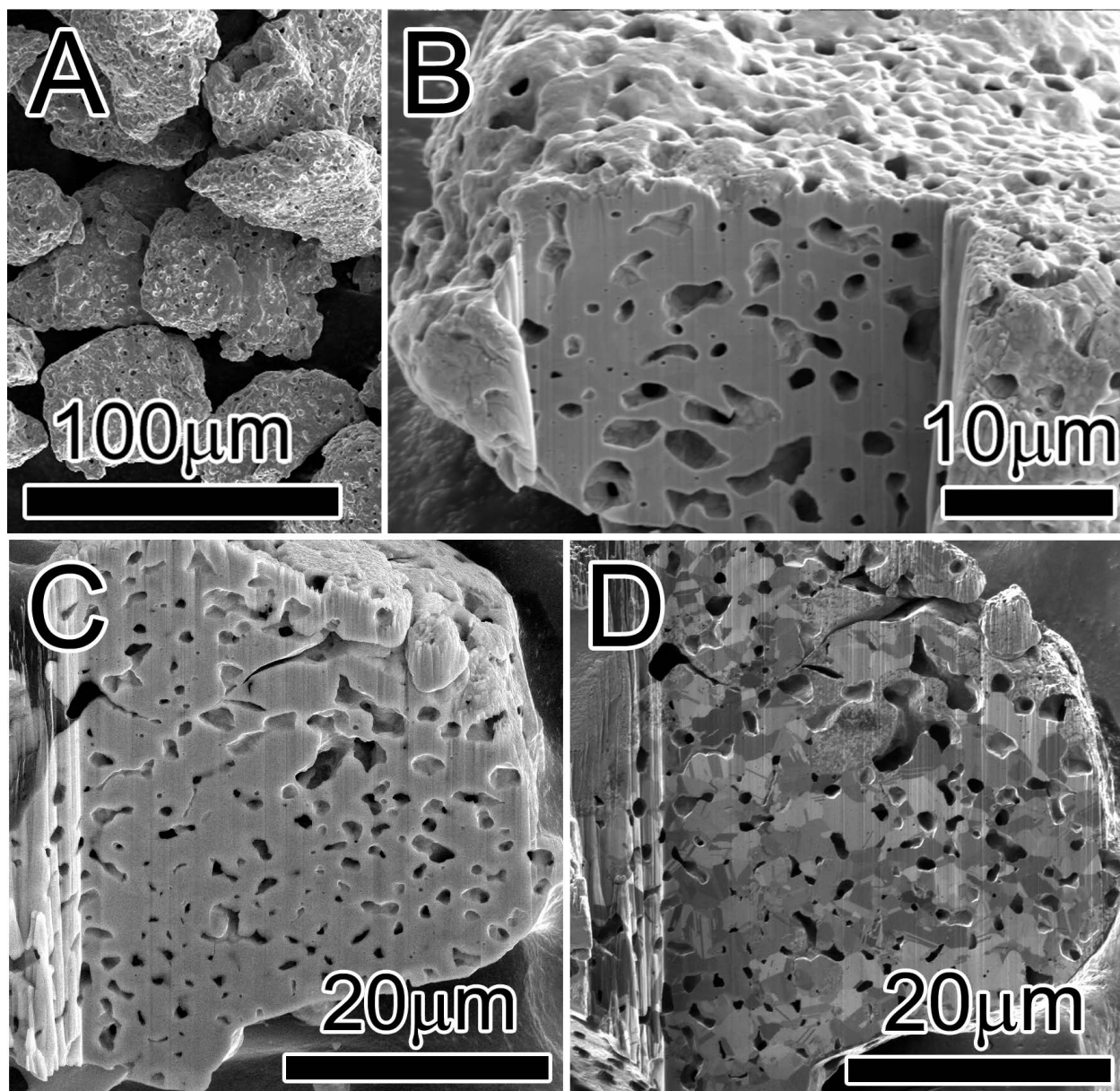


Fig. 1 SEM imaging of powder particles shows the following features: a) loose powder morphology, b) cross section of large powder particle showing porosity extends through the bulk, c) cross section through the center of a powder particle, and d) the corresponding FIBCCI image

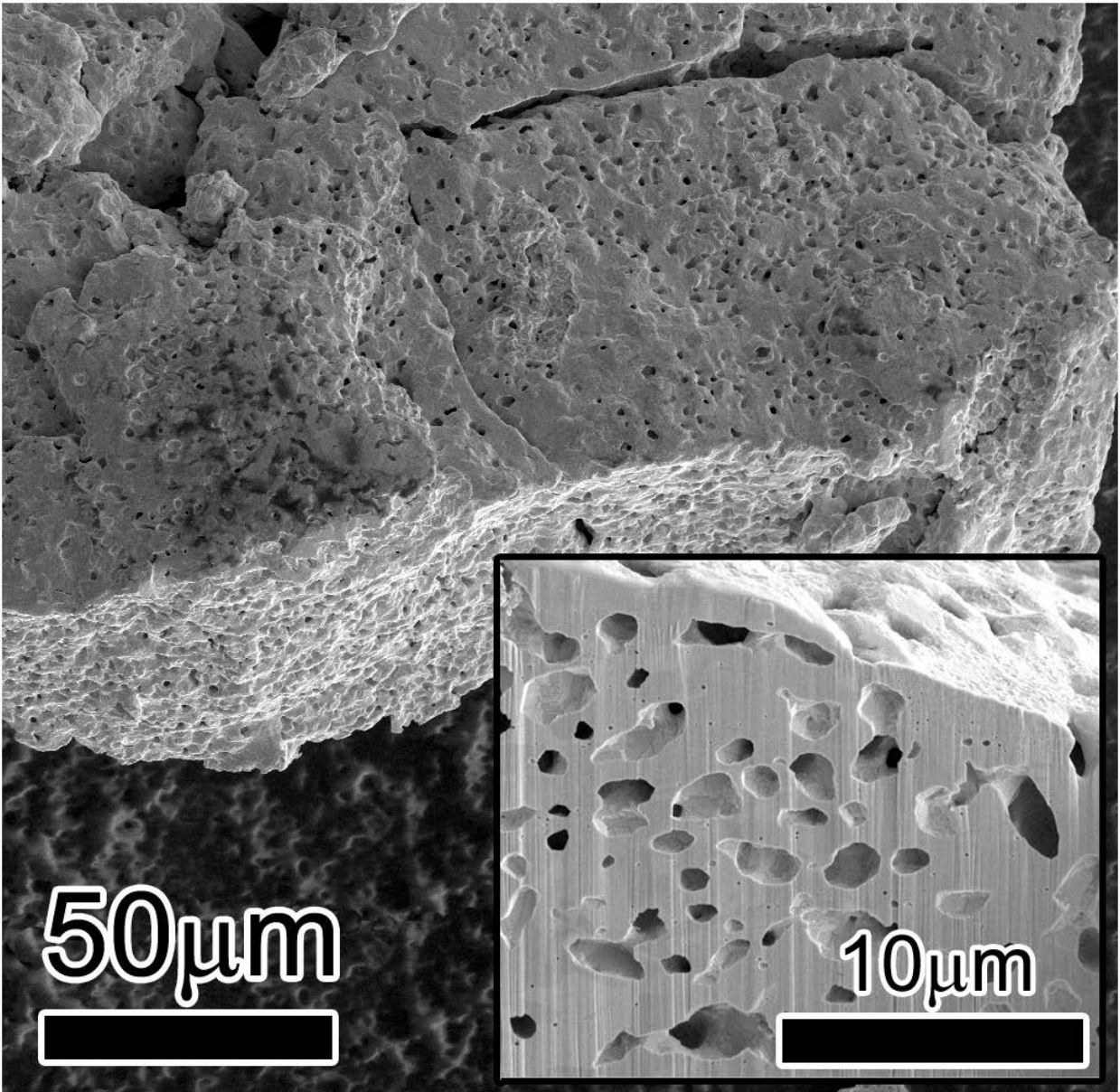


Fig. 2 SEM imaging of powder particles shows porosity intersecting with the surface of the powder. The inset image shows the porosity just below the surface after FIB through a cross section of the particle.

Understanding the microstructure of the Cu alloy at different stages within this process is important because of its relationship with mechanical properties. The mechanical alloying used herein is known to efficiently produce nanocrystalline metals¹⁷ that often exhibit exceptional strengths (e.g., over 10 times greater tensile yield strength for nanocrystalline Cu than for conventional, coarse-grained Cu¹⁸). The as-milled grain size and hardness of the Cu–Sb alloy were 9 nm and 3.5 GPa, respectively, as determined by X-ray diffraction analysis using Scherrer estimation and Vickers microindentation of individual particles. A high-strength matrix will suppress void expansion, but pure nanocrystalline materials are also notoriously sensitive to grain growth at elevated temperature where they rapidly lose their strength (i.e., Cu begins grain growth at 75–100 °C^{19,20}). Herein, we have used a Cu alloy with 5 at% Sb, which has been reported to have increased strengths and thermal stability (a higher grain growth temperature) over pure nanocrystalline Cu.^{21,22} In addition to its influence on grain growth, Sb may also influence the minimum foaming temperature. In a prior study,²¹ Sb was a poor stabilizing agent in nanocrystalline Cu at the expansion temperature of 600 °C applied here, which is potentially related to the large equilibrium solubility of Sb in Cu at elevated temperature (i.e., 5 at% Sb is fully soluble in Cu by approximately 425 °C²³). Additionally, the presence of Sb is thought to enhance solid-state foaming since it dramatically lowers the solidus temperature to approximately 660 °C.

Figure 3 shows a FIB cross section of a foamed particle. FIBCCI was used to determine the grain size within the structure and several features are apparent. First, the grain size is extremely small for a foamed material, with many of the grains being approximately 1–5 μm in diameter. Second, there is an abundance of twins present throughout the bulk of the material. Third, there is a significant presence of nanoscale grains primarily occurring at free surfaces within pores and at the particle exterior (see Fig. 3c). EBSD confirms the small grain size and shows a random texture (Fig. 4). Additionally, dispersive X-ray spectroscopy showed no variation in composition at these locations as compared to the bulk. The engineering of hierarchical features (nanograins, fine, micron grains and pores) in fully foamed parts may lead to a greatly enhanced strength-to-weight ratio and unique applications. Recent reports of similarly graded microstructures resulted in a 2-fold increase in strength with no loss in ductility.²⁴

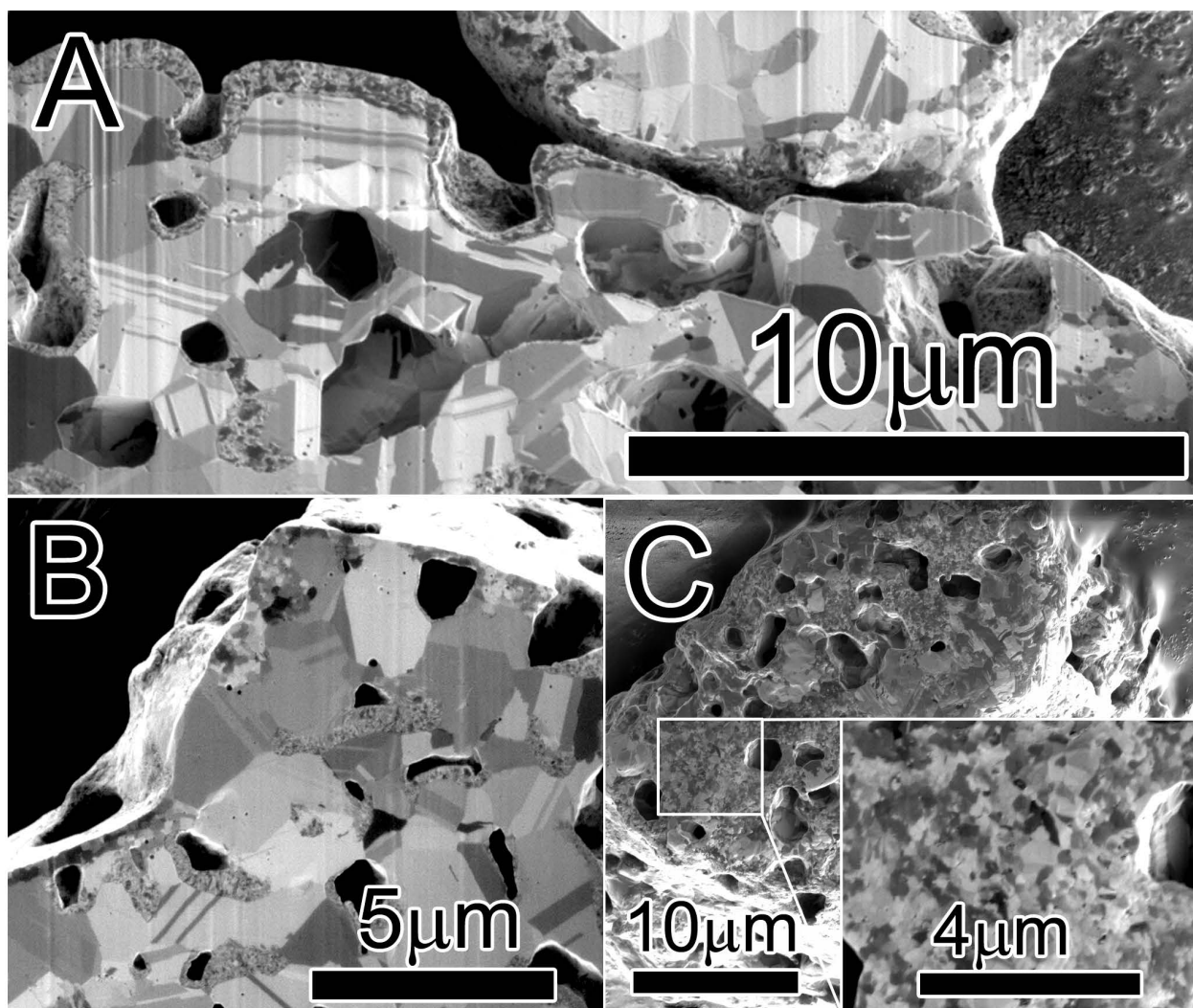


Fig. 3 FIBICC imaging of Cu 5% Sb alloy annealed at 600 °C for 1 h: a) low-magnification image of particle cross section showing considerable porosity, b) high-magnification images showing pore structure, and c) image of particle surface consisting of small grains within magnified inset

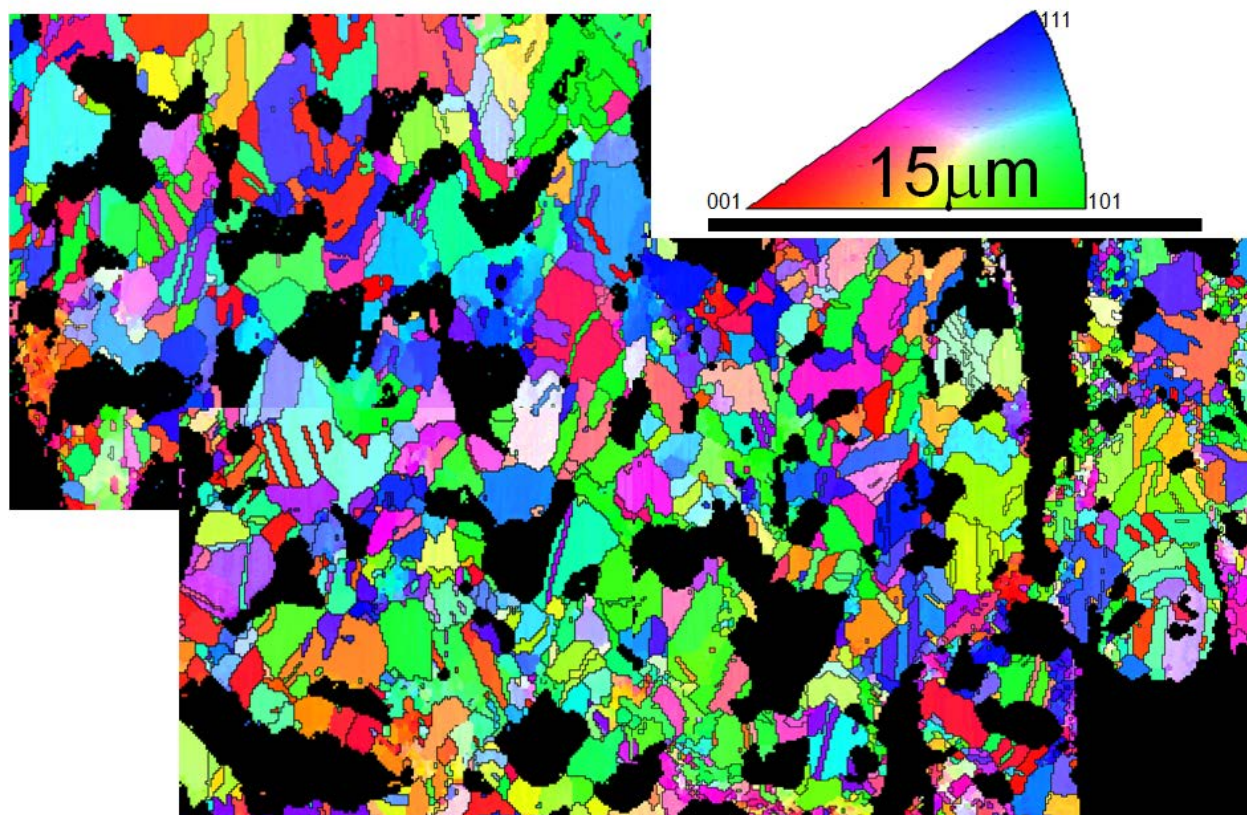


Fig. 4 EBSD of foamed particle cross section. Note the random orientation and the confirmation of a fine grain size at free surfaces.

2.2 Foam Microstructure Characterization

FIB serial sectioning and subsequent image analysis steps were performed to quantitatively describe the nature of porosity in the particles. Figure 5a shows an example of one of the 2-D images collected along with the different stages of analysis necessary to reconstruct the 3-D volume (Fig. 5b). The 4 stages are shown from left to right: 1) initial image, 2) image with manual segmentation, 3) binary image highlighting pores (white) and matrix (black), and 4) fused image with matrix (green), pores (blue), and pore-matrix interface (red). Once the pores were identified, adjacent slices were examined to further refine the image segmentation process. Fifty-one images ($2,048 \text{ pixel} \times 1,768 \text{ pixel}$ area, 12.5-nm/pixel resolution, 250-nm spacing between images) were then used to fully reconstruct the 3-D volume in the particle, as shown in Fig. 5b. The foreground image shows the matrix in green and the background image shows the pore structure in green along with the appropriate dimensions of the 3-D volume.

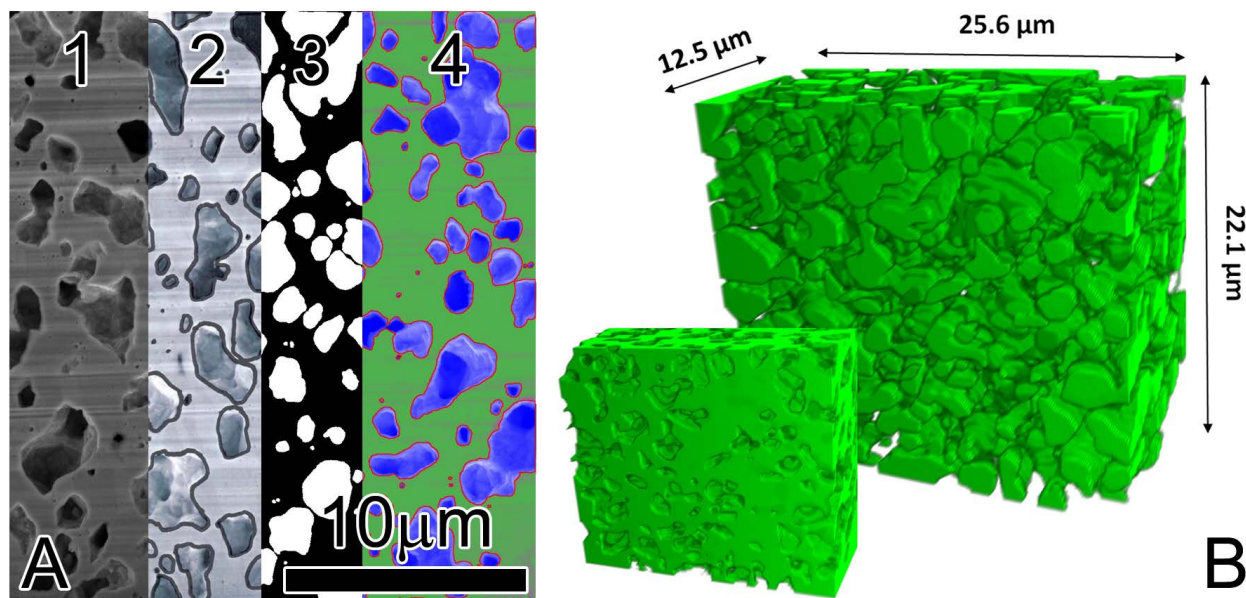


Fig. 5 a) 2-D images showing the different stages of analysis necessary to reconstruct the 3-D volume including image capture, image segmentation, binary image, and fused image. b) 3-D volume reconstruction of matrix structure (foreground) and pore structure (background) within a particle.

A number of porosity statistics can now be ascertained from the 3-D volume. First, the volume fraction porosity of the 3-D foam is 37.1% with a 3.6% standard deviation in pore area fraction from slice to slice. Second, 2-point correlation functions indicate that a representative length scale for correlation in the 2-D slices is on the order of $1\text{--}3 \text{ }\mu\text{m}$, as quantified by the convergence to the square of the area fraction, f^2 , at larger distances. This length scale is in line with calculations of mean equivalent pore diameter ($1.02 \text{ }\mu\text{m}$ for 5,588 pores). Third, the pores in the 2-D slices are

nonspherical, as evaluated from the mean eccentricity value of 0.70 (i.e., 0 is perfectly circular, 1 is a line). This finding is in agreement with studies showing that pore coalescence and interconnectivity results in a more tortuous pore structure.¹⁴ Further supporting this finding, the 3-D connectivity of the pore structure revealed that 92.1% of the porosity is interconnected (i.e., “open” porosity). Last, the mean planar surface area per unit volume from the 2-D images is calculated to be $0.94 \mu\text{m}^2/\mu\text{m}^3$ or $9.4 \times 10^5 \text{ m}^2/\text{m}^3$, which is related to the “true” surface area per volume of $1.2 \times 10^6 \text{ m}^2/\text{m}^3$.²⁵ In fact, this true surface per volume is equivalent to $0.235 \text{ m}^2/\text{g}$, which compares favorably to the experimentally-measured value of $0.390 \text{ m}^2/\text{g}$ (i.e., using the BET method). As permeability is inversely correlated to specific surface area, the high specific surface area of these particles will result in much lower permeabilities.

2.3 Foaming Mechanism

Prior work has shown that cryogenic milling is capable of producing metal foams by a subsequent annealing step.²⁶ In that study, the expansion of the metal was attributed to entrapment of argon (Ar) within the metal structure during milling. This mechanism was proposed because milling was conducted in an Ar atmosphere at liquid nitrogen temperature, where Ar exists in solid form. For the high degree of foaming reported in the present study to occur, we explored an alternative (potentially more plausible) explanation for this phenomenon, which is as follows. The Cu powder used to create the alloy was produced by gas atomization, and the manufacturer’s certificate of analysis reports an oxygen content of approximately 5,000 ppm. Hence, we tested the hypothesis that the expansion mechanism is related to the oxide content of the powder. It is known that oxygen can be incorporated into Cu during atomization, and hydrogen reacts with oxygen during reduction to create steam within particles.²⁷ Copper oxides, which are effectively broken down and distributed during mechanical alloying, are readily reduced under the conditions of the annealing used here.^{28,29} Subsequent annealing under hydrogen causes the reduction of the Cu oxide and the expansion of trapped steam. The oxide reduction and expansion mechanism was preliminarily tested by annealing compacted samples under rough vacuum (better than 1–2 Torr) and comparing the results to the samples annealed in 3% H₂ (balance Ar). Samples annealed under vacuum showed a slight increase in density rather than expanding. This result confirms this hypothesis and suggests that H₂ plays a key role in the expansion process.

2.4 Part Production

The Cu alloy powders were consolidated to assess the level of porosity. There Cu alloy powders were compacted at 0.5, 1, and 2 GPa and the apparent densities after annealing were 2.83 g/cc (31.3% dense), 4.06 g/cc (45.4% dense), and 4.75 g/cc (53.1% dense), respectively. The density

of 31.3% (68.7% porosity) for the 0.5 GPa compact is a remarkable result from a powder metallurgy process, especially because the pore structure is not dominated by necks between sintered particles. The amount of porosity achieved using such a basic process clearly shows that the current limits of solid-state foaming may be reached or even exceeded using the current methodology in association with other solid-state foaming processes.

Although the intraparticle expansion of 35%–40% is similar in extent to the best, traditional creep expansion results, the ability to achieve greater than 65% porosity, the ideal limit of gas entrapment,¹⁴ is a significant accomplishment, especially given the relatively minor deviation from conventional solid-state foaming processes. Since the expansion process is controlled by intraparticle interactions, there are considerable implications for reducing weight and/or improving strengths in bulk engineering structures produced via powder metallurgy. Completely unique to this process is the ability to create foamed powder. This powder can be used in loose form (primary) or in concert with traditional powder metallurgy methods (additive). Specifically, this additional process can potentially add 35%–40% porosity by intraparticle expansion to current solid-state foaming methods such as creep expansion, loose-powder sintering, fugitive templates, and any other method that utilizes a powder feedstock. Moreover, combining porous particles with solid particles may allow engineers to create a graded density and unique properties for a particular application.

The alloy powder was inserted into a pawn-shaped mold and annealed to determine whether simple annealing would be sufficient to generate a sintered part. The resulting part is shown in Fig. 6. The powder was compacted into the mold using only a screw (the threaded passage is apparent at the bottom of the pawn). The detail of the threads and the accurate reproduction of the mold details indicate that this process can be utilized to produce intricate geometries. In light of these results, graded foam structures can be realized by simply blending foaming powders and nonfoaming powders in specific ratios or patterns within a given mold structure. In this manner, the density and consolidated properties can be tailored for a particular application. There can be a number of potential applications if this process is extended to other metals and alloys: custom dental or other biological implants, hydrogen fuel cells, plates or parts for advanced ballistic protection, etc.



Fig. 6 The ease of processing allows for complex parts to be created. This “pawn” was made by filling a 2-piece mold with the Cu alloy powder and applying pressure at one end with a machine screw. The detail of the mold was reproduced with significant accuracy (scale in centimeters).

3. Digital Image Processing

3.1 Imaging Porosity in Foamed Powder Particles

A 10-kV SEM image of a Cu–Sb foamed particle is shown in Fig. 7. The size of this representative particle is on the order of tens of microns, while the porosity (seen breaking through to the surface) is at least an order of magnitude smaller. To visualize the interior porosity of the particle, a FIB was used to slice through the particle at increments of 250 nm. Figure 8a shows the interior porosity for this same Cu–Sb particle. In slicing through the particle, in

addition to interconnected porosity, the particle in Fig. 7 is composed of several particles that have merged together during the mechanical alloying process. It is evident that these were separate particles, because there is porosity associated with the boundary between adjacent merged particles. Figure 8b shows the interior porosity for another Cu–Sb particle. As with the first particle, streaking is observed due to the FIB milling of the foamed particle. To reduce the streaking, subsequent particles were coated with platinum.

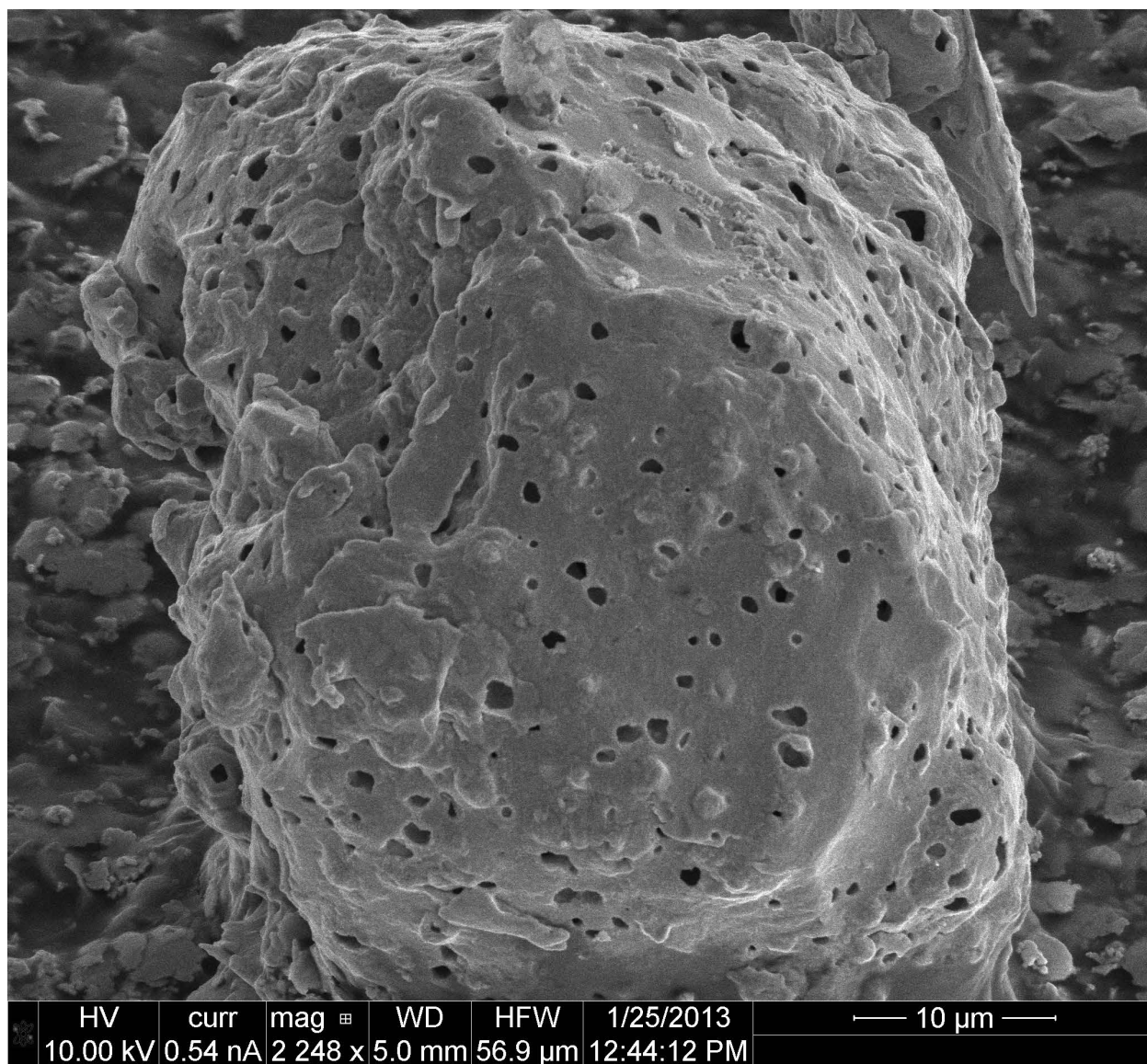


Fig. 7 SEM image of a Cu–Sb foamed particle generated by the solid-state foaming technique

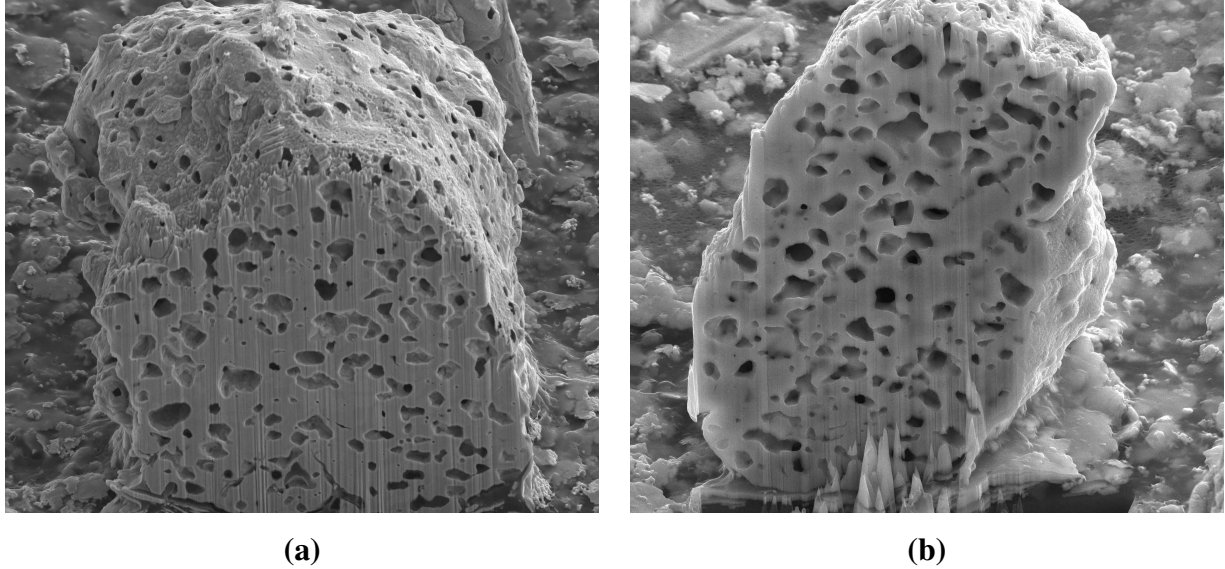


Fig. 8 SEM image of a Cu–Sb foamed particle generated by the solid-state foaming technique: a) same powder particle as that in Fig. 7, and b) second powder particle that exhibits the same pore structure

3.2 3-D Reconstruction Method for Foamed Powder Microstructure

A subsequent smaller area was imaged and FIB milled to produce a 3-D representation of the foam microstructure, an example of which is shown in Fig. 9. The porosity in the image must be segmented to reconstruct the 3-D nature of the porosity and matrix and to characterize the statistics associated with the metal foam. The similar image contrast in the interior of the pores and the streaks complicates the image segmentation process. Traditional digital image processing techniques—including leveling, utilizing fast Fourier transforms (FFTs) to attempt to remove streaks, and various image processing filters—were applied, but were unsuccessful at segmenting the pore microstructure. There are a number of different image processing techniques that could be applied if streaks could be removed from the initial imaging stage, including automated region growing techniques^{30,31} or customized filters/kernels.^{30,32} Future work will investigate techniques (e.g., filling the porosity prior to FIB sectioning, X-ray tomography) for improving image quality to allow for automating the segmentation, reconstruction, and characterization steps.

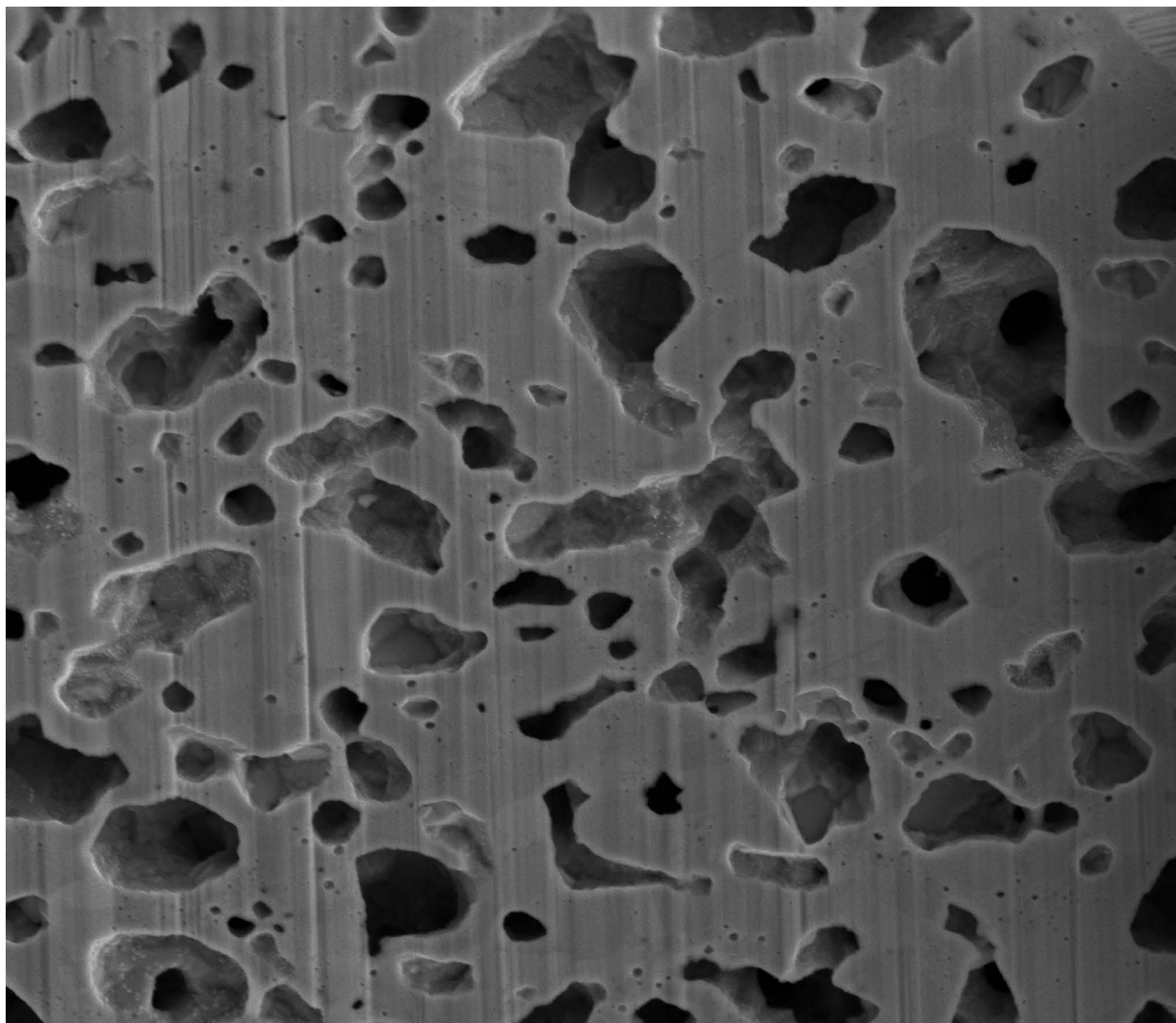


Fig. 9 Close-up SEM image of a Cu-Sb foamed particle generated by the solid-state foaming technique. The ability to observe the pore structure below the FIB surface on the SEM image indicates that these pores appear tortuous (nonspherical) and highly interconnected.

Manual image segmentation was used to delineate the porosity in the foam microstructure. The intensity of a stack of images was rescaled to produce lighter intensities, the images were printed out on standard paper, and users manually traced around the porosity in the sample with a dark marker (Fig. 10). After the porosity was outlined in the images, the images were scanned back into a digital image form and rescaled to original pixel dimensions. The pores contained entirely in the image were traced around the pore boundary. The pores that were cut off by the edge of the image were traced along the pore on the interior of the image and were also traced along the intersection of the pore with the image boundary. In this manner, each pore was entirely enclosed by a black line, which was easily segmented into a binary image and then the enclosed pores were filled using a binary “fill holes” operation. The output binary image is shown in Fig. 11, where white represents a pore region and black represents the metal matrix. To visualize this on the original image, Fig. 12 shows the original image with green denoting the matrix, blue denoting the pores, and red denoting the pore boundaries. To the eye, the manual segmentation process did an adequate job of separating the pore regions from the matrix for further analysis of the microstructure.

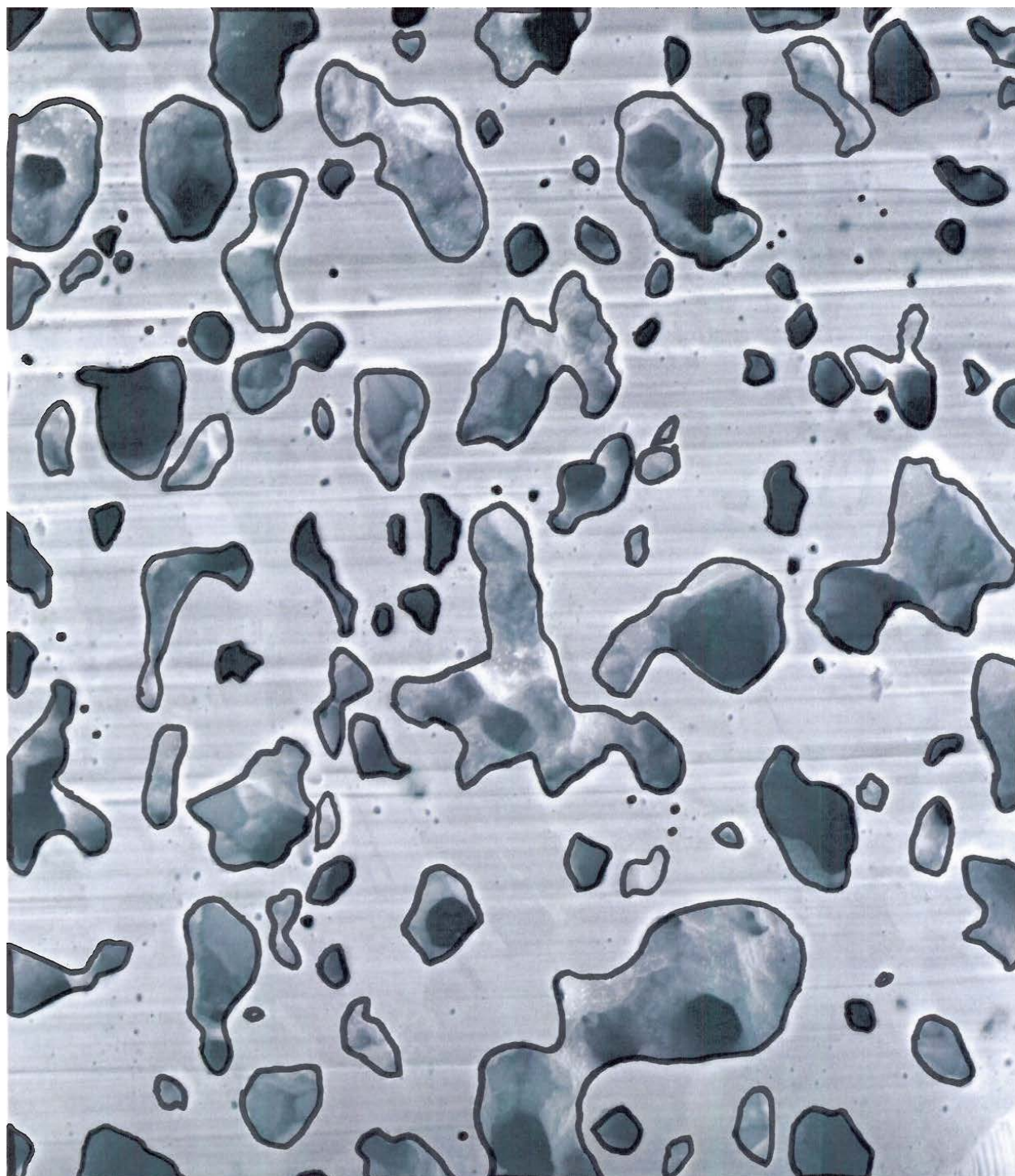


Fig. 10 Manual segmentation of SEM image of a Cu-Sb foamed particle generated by the solid-state foaming technique. After manually tracing the pores, the images were scanned and the pore outlines were automatically identified via image processing.



Fig. 11 SEM binary image of a Cu-Sb foamed particle where black is the matrix and white is the porosity. This binary image can be used for subsequent characterization of the microstructure statistics.

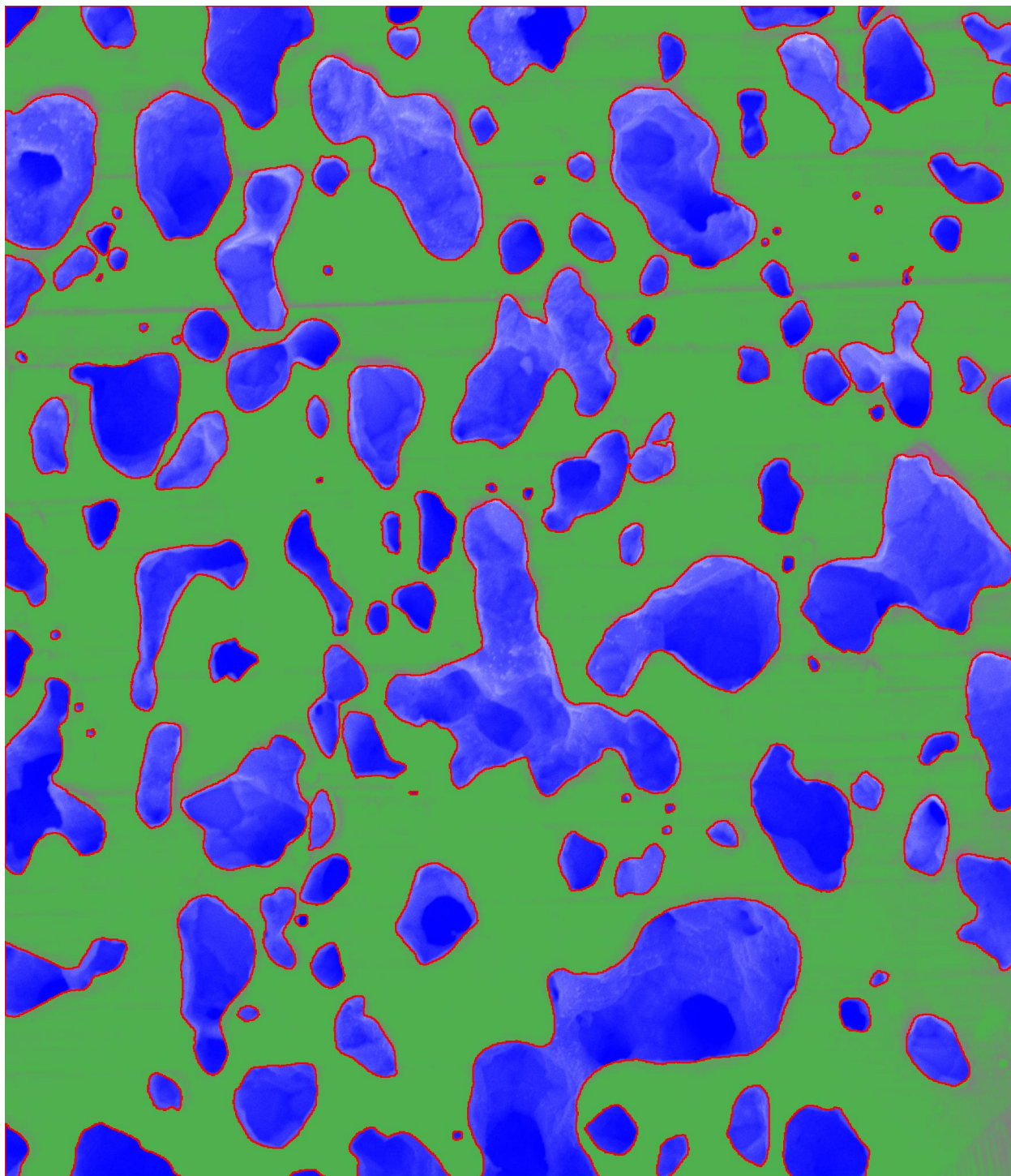


Fig. 12 Segmented SEM image of a Cu-Sb foamed particle where the matrix is green, the pores are blue, and the red lines are the pore boundaries

4. Microstructure Characterization

4.1 Two-Point Correlation Function Definition

The microstructure can now be characterized using 1-point (volume fraction) and 2-point statistics³³ (e.g., 2-point correlation functions^{34–37} and lineal path functions^{38,39}). The lowest order correlation function is the 1-point correlation function, which is the probability that a randomly placed point in a 3-D microstructure is contained in a given phase—this is precisely equal to the volume fraction of that phase, f_i . For a 2-phase microstructure, a 2-point correlation function (TPCF) $P_{ij}(r, \theta, \phi)$ is the probability that a straight line of length r and angular orientation (θ, ϕ) randomly placed in a 3-D microstructure is such that its first end is in the phase i (where, $i = 1$ or 2) and the second end is contained in the phase j (where, $j = 1$ or 2). The variable θ is the angle between the line and the Z-axis of the XYZ reference system, and ϕ is the angle between the projection of the straight line on the XY plane and the X-axis (where the XY plane is the plane of the SEM images and Z is perpendicular to that [FIB direction]). It is important to recognize that the probability associated with a 2-point correlation function only concerns the events at the end points of the line. For a 2-phase microstructure, there are 4 possible TPCFs, namely, $P_{11}(r, \theta, \phi)$, $P_{22}(r, \theta, \phi)$, $P_{12}(r, \theta, \phi)$, and $P_{21}(r, \theta, \phi)$. However, only 1 of the 4 TPCFs is independent, as the following relationships exist.

$$P_{11}(r, \theta, \phi) + P_{22}(r, \theta, \phi) + P_{12}(r, \theta, \phi) + P_{21}(r, \theta, \phi) = 1, \quad (1)$$

$$P_{12}(r, \theta, \phi) = P_{21}(r, \theta, \phi), \quad (2)$$

$$P_{11}(r, \theta, \phi) + P_{12}(r, \theta, \phi) = f_1. \quad (3)$$

Hence, for the following analysis, the TPCF $P_{11}(r, \theta, \phi)$ will be used for $\theta = 90^\circ$ and for 4 values of ϕ ($= \{-45^\circ, 0^\circ, 45^\circ, 90^\circ\}$). In the following analysis, phase 1 is the porosity and phase 2 is the matrix.

TPCFs are often normalized to interpret their results. In many cases, the TPCF is normalized by the volume fraction f_i or the volume fraction squared f_i^2 . Normalizing the TPCF by f_i will force $P_{11}(r, \theta, \phi) \rightarrow 1$ as $r \rightarrow 0$ (since the TPCF $P_{11}(r)$ will approach the volume fraction f_1 at infinitely small distances). Normalizing the TPCF by f_i^2 will force $P_{11}(r, \theta, \phi) \rightarrow 1$ as $r \rightarrow \infty$. This normalization approach (TPCF/ f_i^2) is often used because, at large distances, there is no

correlation between the 2 points and the probability is solely determined by the probability of obtaining that particular phase.

$$P_{11}^*(r, \theta, \phi) = \frac{P_{11}(r, \theta, \phi)}{f_1^2}. \quad (4)$$

There are 2 different scenarios that can occur with 2-point correlation functions: a scenario where the image is nonperiodic (i.e., an experimental microstructure image) and a scenario where the image is periodic (i.e., a reconstructed microstructure). Example MATLAB scripts for calculating TPCFs in either case are included in Appendixes A and B. Appendix A contains 2 different methods of calculating TPCFs—with and without using FFTs—to verify that the FFT method is giving the appropriate statistics.

4.2 Lineal Path Function Definition

The lineal path function (LPF)^{38,39} $L_{ii}(r, \theta, \phi)$ is the probability that a line of length r located randomly in a microstructure is entirely in phase i . This parameter gives more insight into the connectivity and clustering tendencies of certain phases (i.e., porosity). We are interested in LPFs for porosity along directions identical to the TPCF case. Similar to the TPCF, the LPF can be normalized to aid in analysis. For instance, it might be informative to compare the LPF to the probability that there could be a random occurrence of a particular phase in succession, i.e.,

$$L_{11}^*(r, \theta, \phi) = \frac{L_{11}(r, \theta, \phi)}{f_1^n}, \quad (5)$$

where n is the number of connected phases contained in line of length r . For instance, the LPF would be divided by f_i^2 for 2 connected phases in a row, f_i^3 for 3 connected phases in a row, etc. This normalization would be informative for ascertaining whether the connectivity is merely a function of a random microstructure of a certain volume fraction ($L_{11}^*(r, \theta, \phi) \leq 1$) or whether it is a trait of the microstructure ($L_{11}^*(r, \theta, \phi) > 1$). However, since most microstructures are not random and do display some level of connectivity, which would cause $L_{11}^*(r, \theta, \phi)$ to increase until $L_{11}^*(r, \theta, \phi) = 0$, the LPF $L_{11}(r, \theta, \phi)$ is often a more informative metric. Similar to TPCFs, there are 2 different scenarios that can occur: periodic and nonperiodic images. An example MATLAB script for calculating LPFs in nonperiodic images is included in Appendix C. Both 2-point statistics were used to characterize the spatial arrangement of porosity within the foam, since the TPCF represents the spacing between porosity and the LPF represents the connectivity of porosity.

The difference between the TPCF $P_{11}(r)$ and the LPF $L_{11}(r)$ (for arbitrary $\{\theta, \phi\}$ direction) is schematically depicted in Fig. 13. For this schematic, a 1-D representation of 2 phases was chosen as it corresponds to this report, i.e., porosity in gray boxes and matrix in white boxes. Figure 13 shows the combination of boxes that are accounted for in both the TPCF $P_{11}(r)$ and LPF $L_{11}(r)$ for distances of $r = 1, r = 2$, and $r = 3$. First, notice that as the distance increases, the number of possible combinations for the TPCF increases. Recall that the TPCF does not consider the boxes in between; only the boxes at the end of the line. However, the LPF requires that all boxes along the line belong to a particular phase; therefore, the probability of this occurring decreases with increasing distance. Additionally, this schematic shows that the TPCF represents the spacing between porosity while the LPF represents the connectivity of porosity. This example is the same concept as that used to calculate the 2-point statistics $P_{11}(r, \theta, \phi)$ and $L_{11}(r, \theta, \phi)$ for the 3-D reconstructed microstructure.









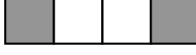



	TPCF, $P_{11}(r)$	LPF, $L_{11}(r)$
$r = 1$		
$r = 2$	 	
$r = 3$	   	
	 Phase 1	 Phase 2

Fig. 13 One-dimensional schematic showing the difference between TPCF $P_{11}(r)$ and LPF $L_{11}(r)$ for distances of $r = \{1, 2, 3\}$

4.3 One-Point and Two-Point Statistics of Foamed Powder Particles

4.3.1 One-Point Statistics

There are a number of different 1- and 2-point microstructure statistics that can be computed from the reconstructed microstructure. In terms of 1-point statistics, the area fraction or volume fraction f_i is most common. Figure 14 is the variation in the area fraction as a function of the segmented slices through the reconstructed dataset. The average f_i line for the 3-D microstructure is shown ($\mu = 37.1\%$) as well as the 1 standard deviation lines ($\mu \pm \sigma = 37.1\% \pm 3.6\%$).

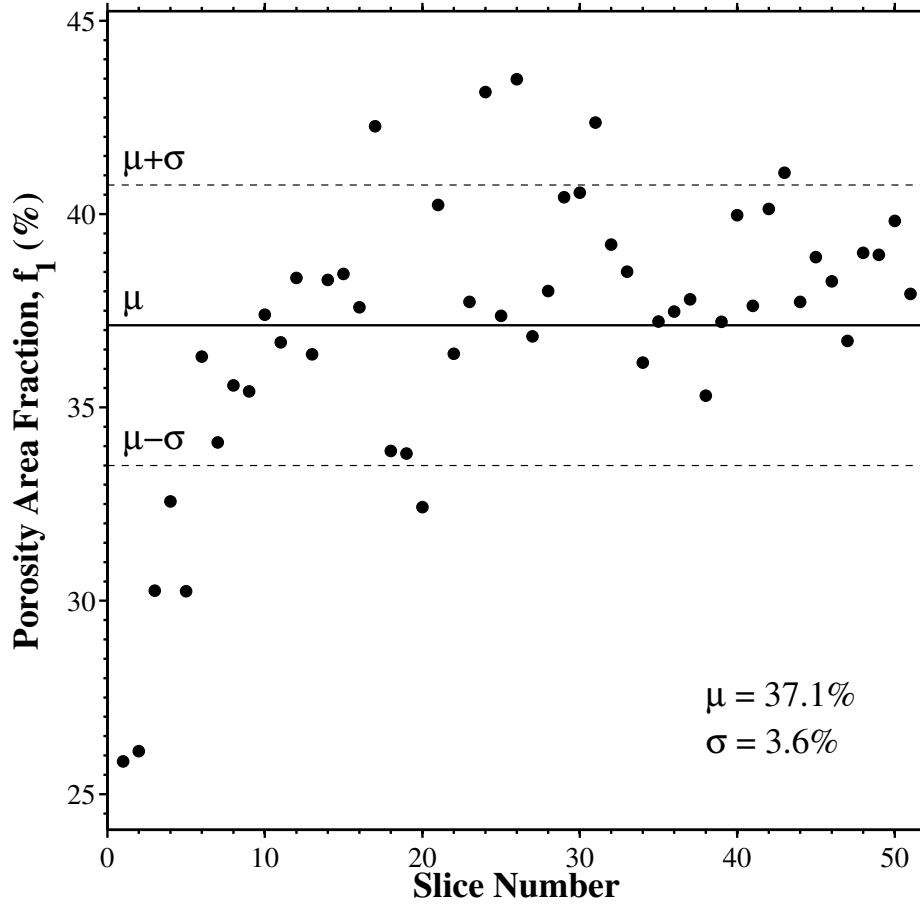


Fig. 14 The variation in area fraction as a function of the FIB slices through the 3-D dataset

An additional method for examining the microstructure using 1-point statistics is to segment each image into multiple windows with a particular size. This method allows the calculation of multiple area fractions within a single image and examines the variation in this area fraction distribution as a function of window size (length scale). This concept is a premise for the multiscale analysis of area fractions code,^{40–42} which can calculate the isotropic⁴⁰ and

directional⁴¹ representative length scales of microstructures using only 1-point statistics. The representative length scales (for anisotropic microstructures) or representative volume elements of various microstructure features may provide insight into material properties.

4.3.2 Two-Point Correlation Function Statistics

The TPCFs $P_{11}(r, \phi)$ for the 4 directions were calculated for the foam microstructure. Figure 15 is an example of the TPCFs for $\theta = 0^\circ$, showing the variability in the TPCF as a function of slice and distance. Moreover, this shows that normalizing the TPCF for each slice can help show convergence of the TPCF (to random behavior) beyond the microstructural length scale.

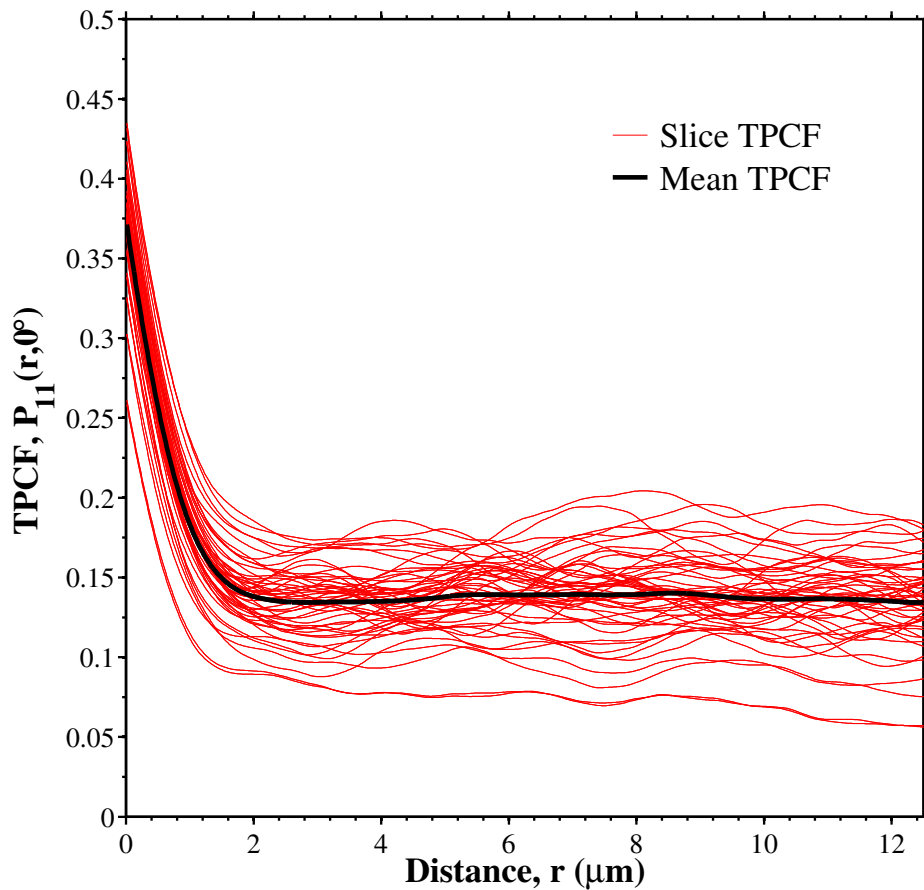


Fig. 15 TPCF as a function of distance for $\theta = 0^\circ$ (enlargement of Fig. 16a). The red curves denote the TPCFs from the different slices and the black curve is the mean TPCF throughout the entire 3-D dataset.

Figure 16 shows the TPCF for all 4 directions, wherein each slice represents a red curve and the black curve is the mean TPCF over the entire 3-D dataset. The distribution of different starting points for each slice is representative of the different area fractions for each slice (i.e.,

$P_{11}(r=0) = f_1$). At large distances ($r \geq 4 \mu\text{m}$), the convergence to a particular value of P_{11} (with fluctuations) is due to the randomness of the microstructure (which corresponds to the area fraction squared f_i^2) rather than any true correlation between the porosity. Therefore, it is instructive to normalize the TPCF by dividing by the area fraction squared f_i^2 , which will be used in the subsequent analysis of TPCFs.

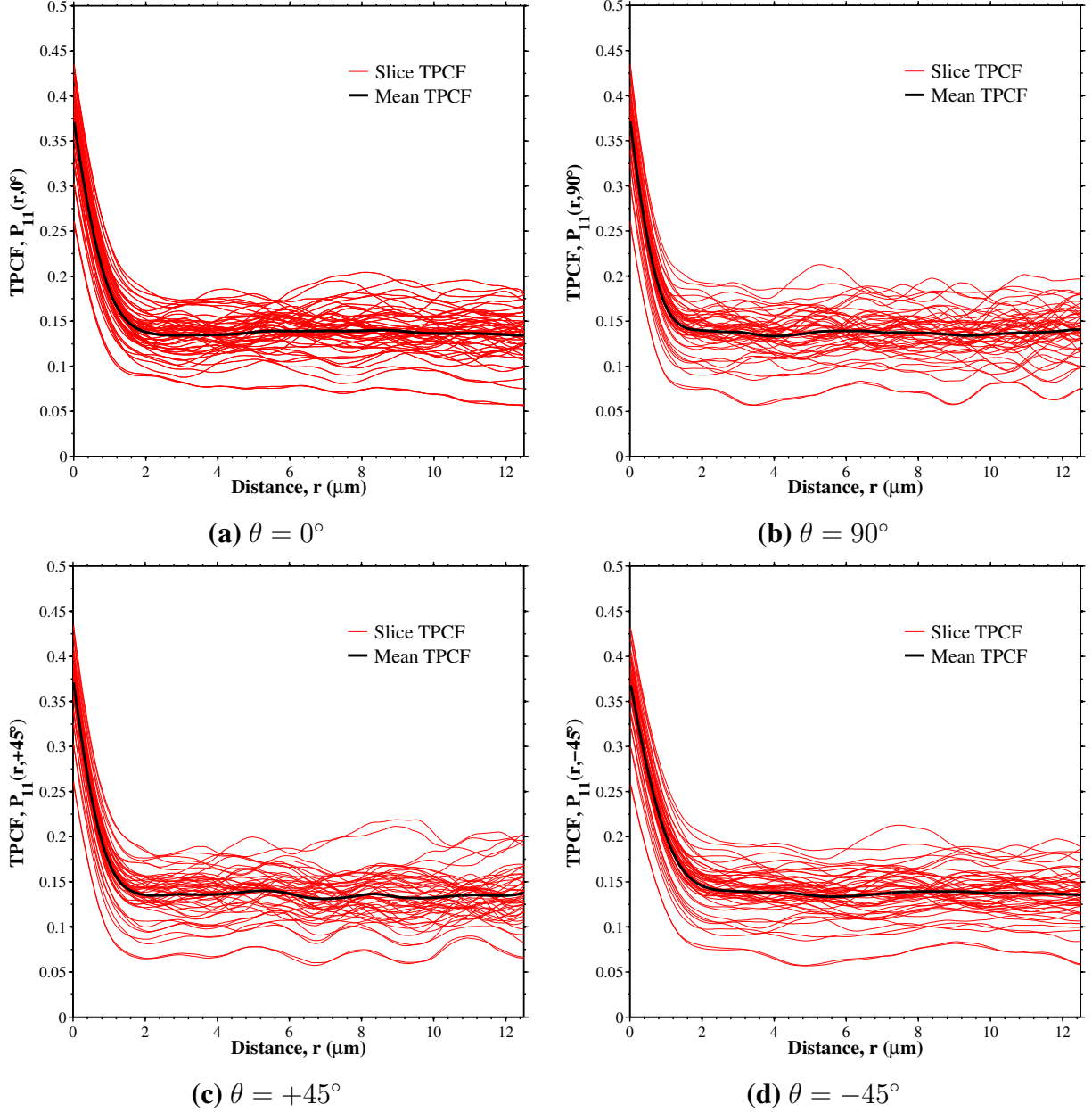
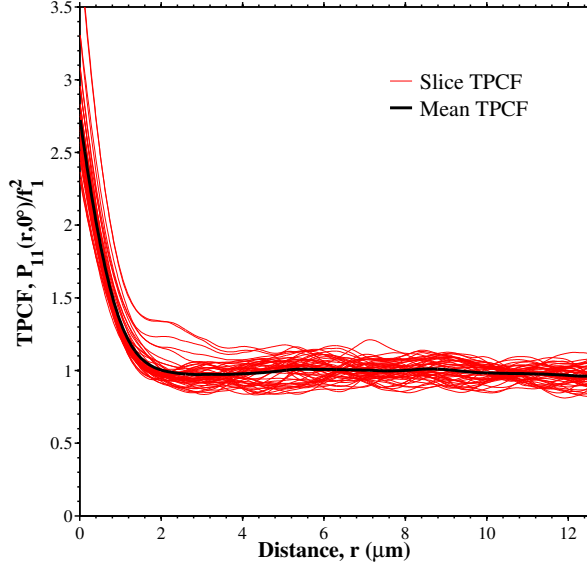
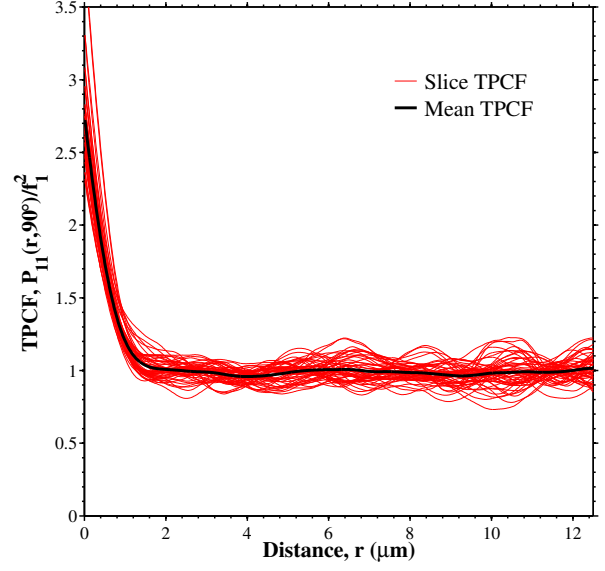


Fig. 16 TPCF as a function of distance for θ of a) 0° , b) 90° , c) $+45^\circ$, and d) -45° . The red curves denote the TPCFs from the different slices and the black curve is the mean TPCF over the entire 3-D dataset in the various directions.

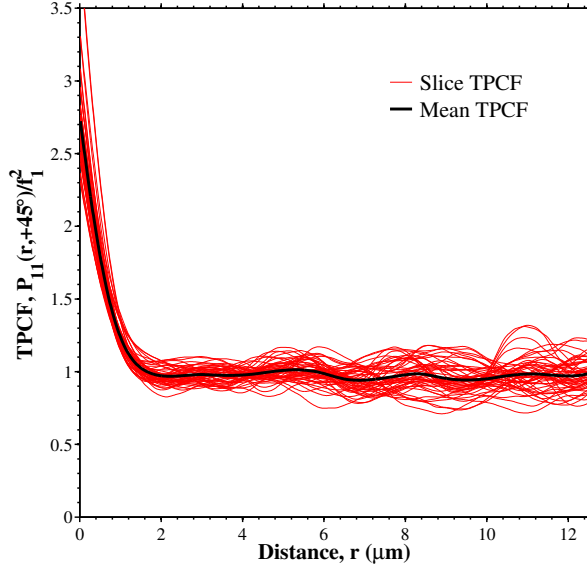
Figure 17 shows the normalized TPCF for all 4 directions, wherein each slice represents a red curve and the black curve is the mean TPCF over the entire 3-D dataset. Another way to visualize the combined information from the different slices is calculate the standard deviation of the normalized TPCF and plot this along with the mean behavior for the entire microstructure (Fig. 18). In both cases, notice that the Y-axis represents the normalized TPCF (divided by f_1^2) and that the mean TPCF approaches a value of 1 at less than 2 nm. This length scale represents a representative length scale for the microstructure, since after 2 nm, the probability that there is any correlation with a phase greater than 2 nm is purely random. Moreover, the similarity between the TPCFs in the different directions (i.e., the different subfigures) indicates that the microstructure is isotropic. This is further substantiated by overlaying the mean TPCFs and 1-standard-deviation curves (dashed lines) on 1 plot (Fig. 19).



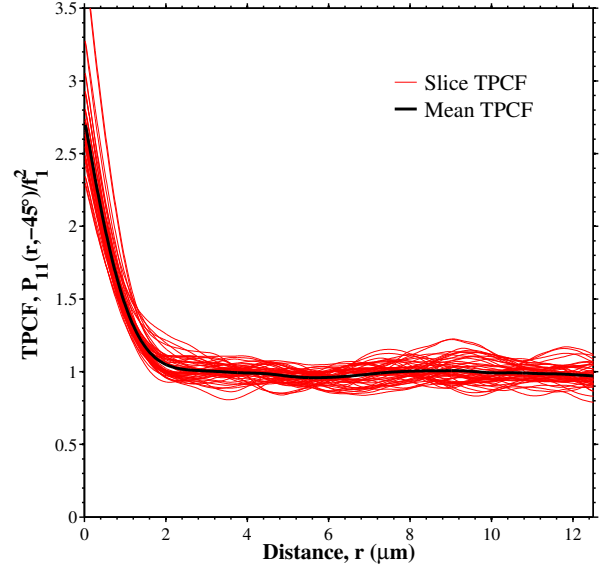
(a) $\theta = 0^\circ$



(b) $\theta = 90^\circ$



(c) $\theta = +45^\circ$



(d) $\theta = -45^\circ$

Fig. 17 Normalized TPCF as a function of distance for θ of a) 0° , b) 90° , c) $+45^\circ$, and d) -45° . The red curves denote the TPCFs from the different slices and the black curve is the mean TPCF over the entire 3-D dataset in the various directions.

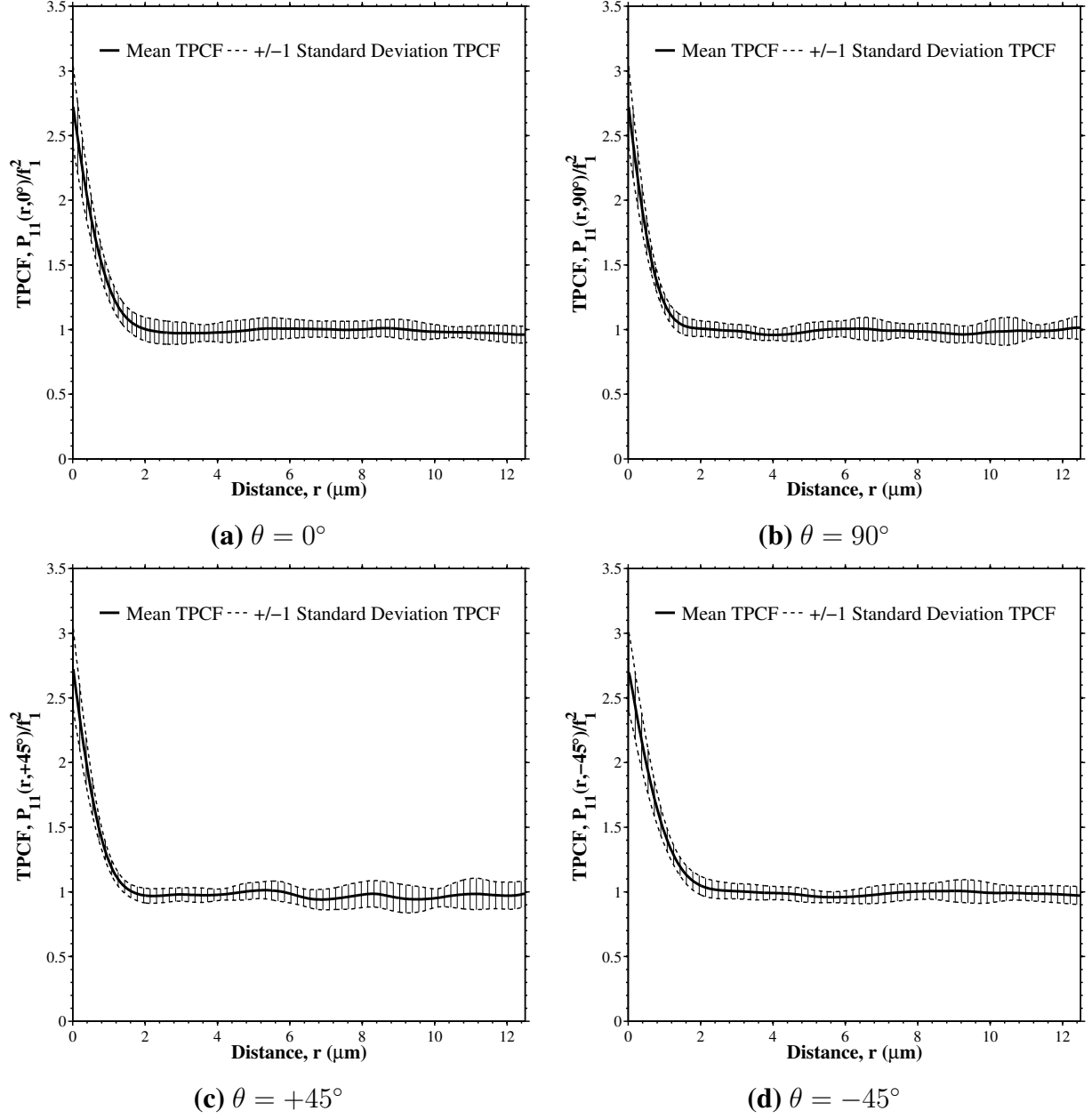


Fig. 18 Normalized TPCF as a function of distance for θ of a) 0° , b) 90° , c) $+45^\circ$, and d) -45° . The dashed lines bounding the mean TPCF represent 1 standard deviation from the mean.

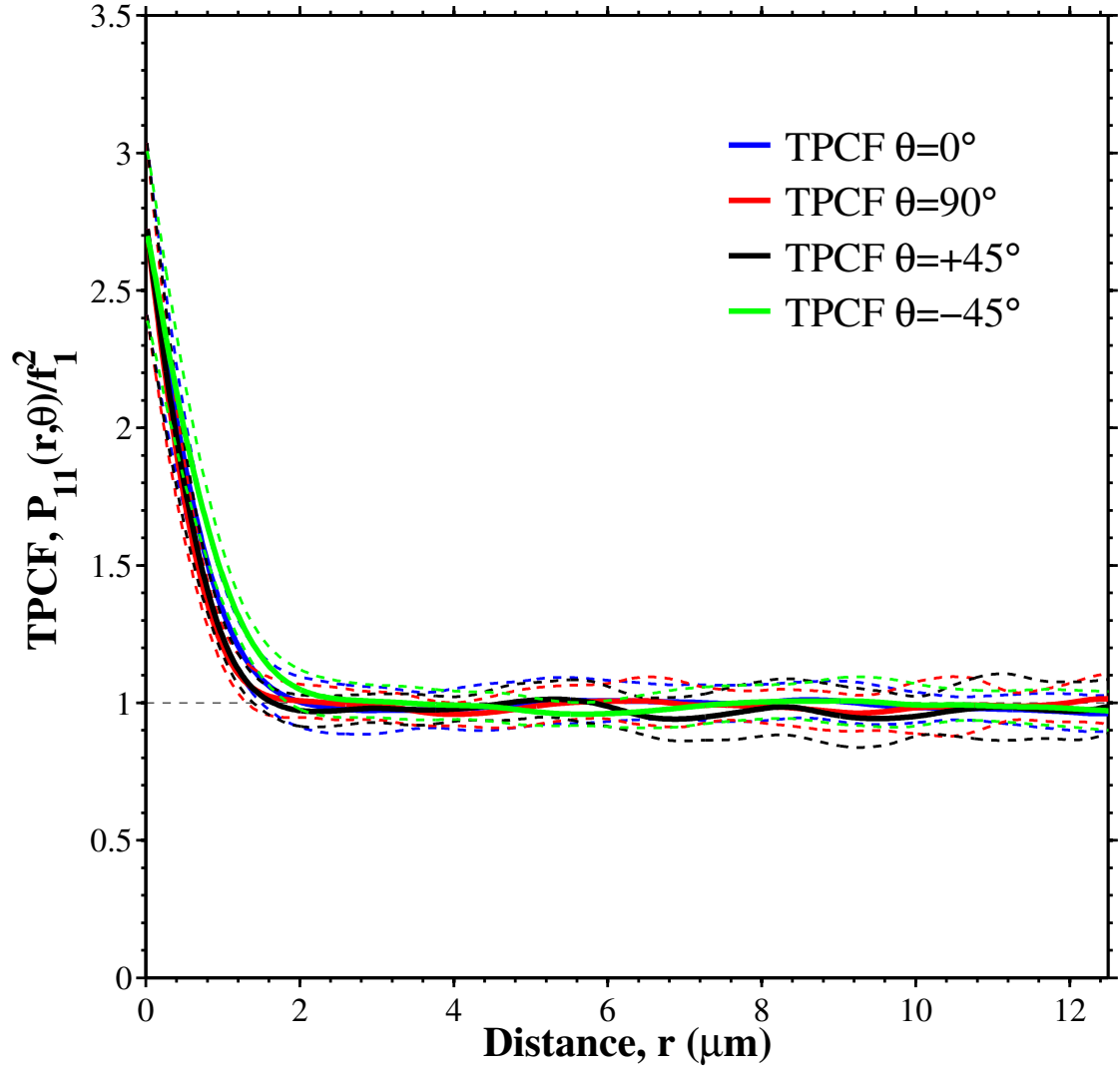


Fig. 19 The mean normalized TPCFs for the 4 directions along with the 1 standard deviation lines. The microstructure approaches $P_{11} = 1$ within 2 μm . Beyond 2 μm , the TPCF approaches that given by the area fraction of porosity squared (i.e., f_1^2), i.e., a purely random correlation between porosity.

A more quantitative method to define and compare representative length scales would be to identify the length scale at which the TPCF is some percentage above that of a random correlation between phases (i.e., $P_{11}/f_1^2 = 1$). Figure 20 shows a magnified view of the preceding plots for porosity over the range surrounding the critical distance (qualitative) of 2 nm. Using a critical normalized TPCF value of either 1.1 or 1.5 results in length scales that are on the order of 1.5 μm and 0.8 μm , respectively. There is some degree of scatter between the different directions, which indicates that there may be a small degree of anisotropy to the microstructure.

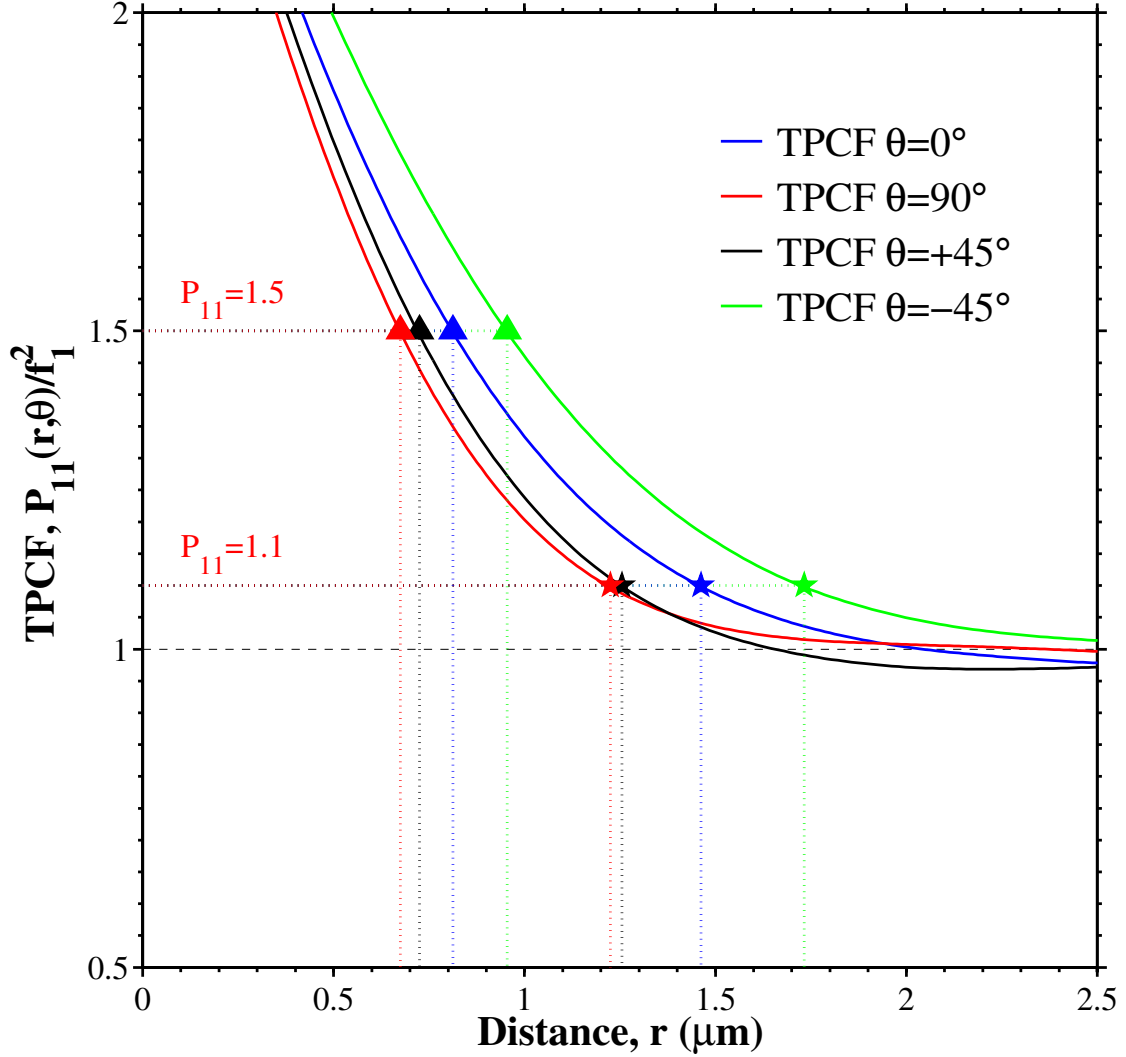


Fig. 20 The mean normalized TPCFs for the 4 directions along with the representative length scales given by the TPCF intersection with $P_{11} = 1.1$ and $P_{11} = 1.5$ for the porosity

A similar quantitative analysis of microstructure length scales using TPCFs was performed on the Cu–Sb matrix as well. Figure 21a–d has similar variability in the slice TPCFs for the 4 different directions (0° , 90° , $+45^\circ$, and -45° , respectively). The mean TPCFs for the directions can use the

same critical TPCF values (1.1 and 1.5) to assess the microstructure length scales. A few observations can be made about Fig. 21. First, the normalized TPCF scale is much smaller than for the porosity. Recall that the TPCF is normalized by f_i^2 so that the TPCF will go to unity as the TPCF approaches the same probability as that of 2 phases at distance r randomly occurring. Since the matrix volume fraction is much greater than that of the porosity, lower normalized TPCF values are expected at small distances. Second, the critical normalized TPCF value of either 1.1 or 1.5 results in length scales that are on the order of 1.0 μm and 0.3 μm , respectively. This length scale is much lower than that for the porosity at the same normalized TPCF values. This function is again influenced by the volume fraction f_i in the normalization—the higher volume fraction means that there is a greater probability of random occurrence of Cu–Sb matrix in the microstructure at distance r , which leads to lower critical length scales. In both the porosity and matrix analyses using the aforementioned methodology, the critical length scale is on the order of 1 μm , though, which again reinforces the small scale of the porosity using the present solid-state foaming process.

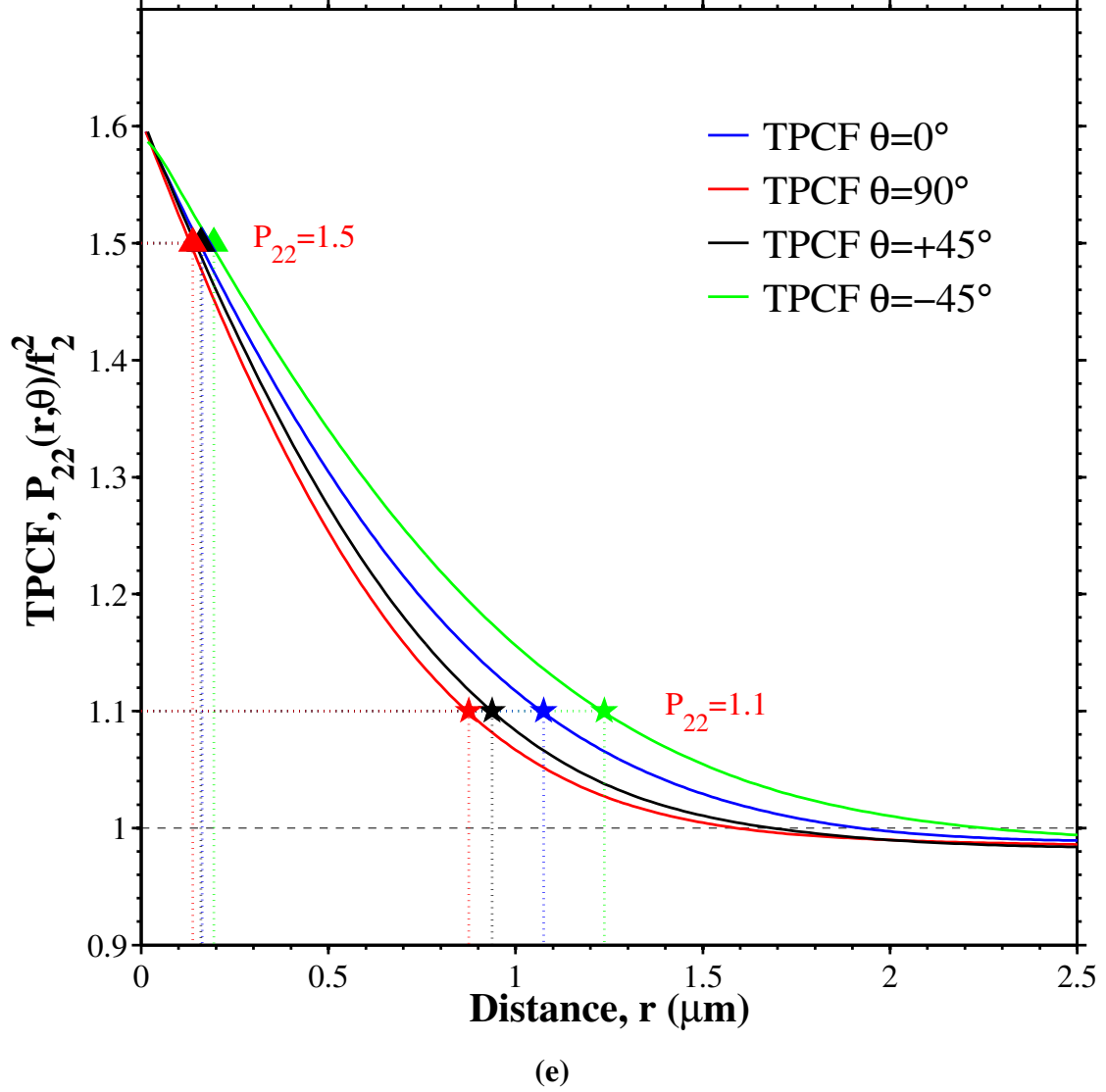
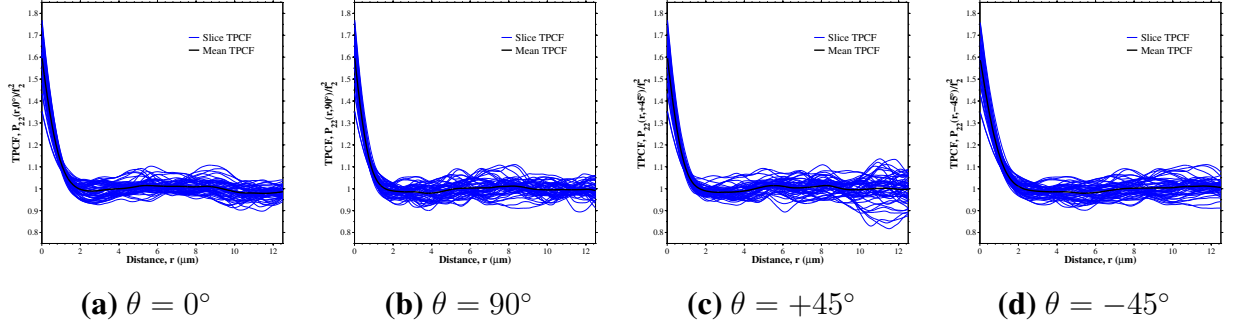


Fig. 21 The normalized TPCFs for the matrix phase for the 4 directions for the slices shows similar variability and length scales as the porosity TPCFs (a–d). The mean TPCFs for the matrix in the 4 directions was computed along with the representative length scales given by the TPCF intersection with $P_{22} = 1.1$ and $P_{22} = 1.5$ (e).

4.3.3 Lineal Path Function Statistics

The lineal path function is another way of statistically characterizing the microstructure. Whereas the TPCFs assess the spacing of microstructure features, the LPFs assess the connectivity of the microstructure. Figure 22 shows slice and mean LPFs for 0° (a,c) and 90° (b,d) in the porosity (a,b) and the Cu matrix (c,d). Here, the lineal path function is not normalized at all. Hence, the lineal path function is the probability that a line of length r will completely lie within the phase. As the line length increases, there is a lower probability that this will occur. In a similar manner to the TPCF, a critical LPF value can be used to compare length scales. For instance, critical LPF values of either 0.25 (25%), 0.10 (10%), or 0.01 (1%) result in length scales (from the 0° LPF plots) of approximately 0.4 μm , 1.2 μm , and 2.9 μm for the porosity and approximately 1.6 μm , 3.3 μm , and 7.2 μm for the matrix, respectively. The values for the 90° LPFs are listed in the plots as well. Therefore, the length scales of the matrix microstructure are on the order of 2–3 times that of the porosity.

The LPFs indicate that the microstructure is far from random at these scales. The spacing between pixels in the microstructure is such that there are 80 pixels in 1 μm . Except for the highest volume fractions, it is very unlikely that 80 pixels picked at random will result in the same phase. For example, the probability of randomly obtaining a line length of 0.1 μm (100 nm, 8 pixels) with a volume fraction of 37% (porosity) or 63% (matrix) is 0.035% and 2.482%, respectively. Increasing this line length to 0.2 μm (200 nm, 16 pixels) results in a probability of 1.2e-05% and 0.062%, respectively. Comparing these values to the computed LPFs at 0.1 μm in Fig. 22 shows that the probabilities calculated indicate that the microstructure is far from random at these scales.

The 2-point correlation statistics and lineal path statistics can be important for reconstruction of microstructures that are statistically representative of the original microstructure.^{43–45} While microstructures can be reproduced with 2-point correlation statistics, recent studies have shown that, in some cases, this can lead to microstructures that approximate the TPCFs used in the objective function of the optimization process, but fail to yield similarity to the initial microstructure.⁴³ Hence, it is often necessary to characterize multiphase microstructures with both TPCFs and LPFs.

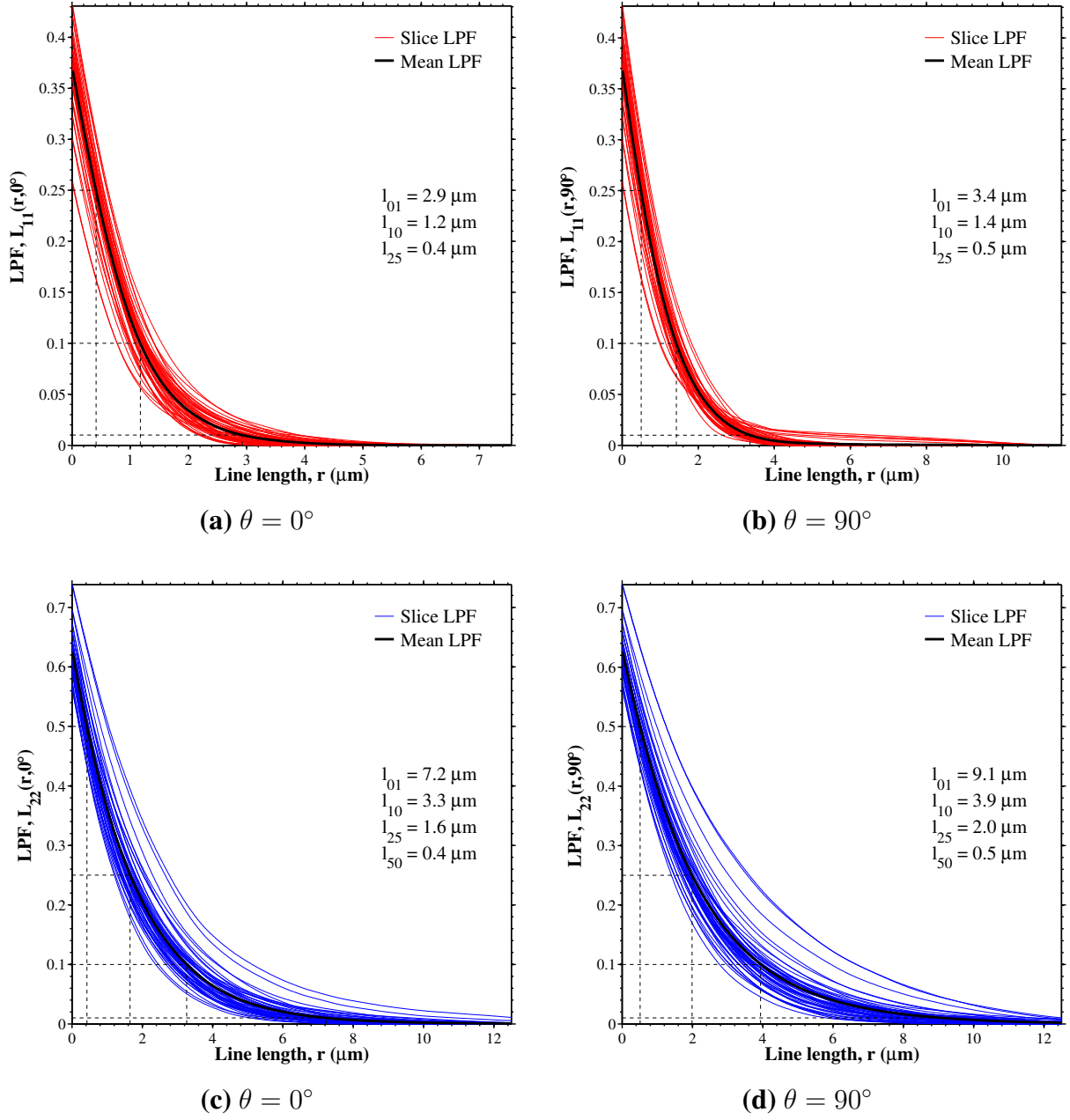


Fig. 22 LPF as a function of distance for θ of 0° (a,c); 90° (b,d); for the porosity, i.e., $L_{11}(r, \theta)$ (a,b); and the matrix, i.e., $L_{22}(r, \theta)$ (c,d). The colored lines are the LPF computed from individual slices (red for porosity, blue for matrix) and the dashed lines show the calculation of the length scale for particular values of the LPF.

5. Conclusions

A process has been developed for creating Cu foams with porosities in excess of 65% by an intraparticle expansion solid-state foaming process combined with powder sintering.⁴⁶ The relatively simple technique involves only 2 steps: milling the powder and then annealing it in a reducing atmosphere. The working hypothesis is that oxides within the particles are reduced during annealing, creating steam that expands into microscale voids. The porosity is very fine, averaging 1 μm in diameter, and is characterized by a nonspherical morphology. After 1 h at 600 °C, the pores show extensive coalescence and percolation (greater than 90% open porosity). The microstructure of the Cu alloy features a fine grain size complete with twins, and an ultrafine to nanoscale grain size at many of the free surfaces. The ability to apply this technique in creating a small part by sintering was demonstrated. It is expected both the process and product are industrially scalable.

Furthermore, this report details the methods by which the powders were sectioned by FIB, imaged with the SEM, and analyzed using a combination of digital image processing and microstructure characterization methods. One- and 2-point statistics were used to characterize the microstructures. The TPCFs (lineal path functions) denote that the spacing (connectivity) between the 2 phases is on the order of 1–3 μm . Future work will examine enhancements to the processing of these solid-state foams as well as improvements in the ability to automate the imaging and characterization processes.

6. References

1. Ashby MF, Lu TJ. Metal foams: a survey. *Science in China Series B*. 2003;46(6):521–532.
2. Lefebvre LP, Banhart J, Dunand DC. Porous metals and metallic foams: current status and recent developments. *Advanced Engineering Materials*. 2008;10(9):775–787.
3. Davies P. The inflationary universe – was the cosmos born in a fleck of foam. *Sciences-New York*. 1983;23(2):32–37.
4. Banhart J. Metal foams: Production and stability. *Advanced Engineering Materials*. 2006;8(9):781–794.
5. Dunand DC. Processing of titanium foams. *Advanced Engineering Materials*. 2004;6(6):369–376.
6. Nam D, Kim R, Han D, Kim J, Kwon H. Effects of $(\text{NH}_4)_2\text{SO}_4$ and BTA on the nanostructure of copper foam prepared by electrodeposition. *Electrochimica Acta*. 2011;56(25):9397–9405.
7. Xie S, Evans JRG. High porosity copper foam. *Journal of Materials Science*. 2004;39(18):5877–5880.
8. Simone AE, Gibson LJ. The tensile strength of porous copper made by the GASAR process. *Acta Materialia*. 1996;44(4):1437–1447.
9. Lu HB, Li Y, Wang FH. Synthesis of porous copper from nanocrystalline two-phase Cu-Zr film by dealloying. *Scripta Materialia*. 2007;56(2):165–168.
10. Kim JH, Kim RH, Kwon HS. Preparation of copper foam with 3-dimensionally interconnected spherical pore network by electrodeposition. *Electrochemistry Communications*. 2008;10(8):1148–1151.
11. El-Hadek M, Kaytbay S. Mechanical and physical characterization of copper foam. *International Journal for Mechanics and Materials in Design*. 2008;4:63–69.
12. Kearns MW, Blenkinsop PA, Barber AC, Farthing TW. Manufacture of a novel porous metal. *International Journal of Powder Metallurgy*. 1988;24(1):59–64.

13. Murray NGD, Schuh CA, Dunand DC. Solid-state foaming of titanium by hydrogen-induced internal-stress superplasticity. *Scripta Materialia*. 2003;49(9):879–883.
14. Elzey DM, Wadley HNG. The limits of solid state foaming. *Acta Materialia*. 2001;49(5):849–859.
15. Li HL, Oppenheimer SM, Stupp SI, Dunand DC, Brinson LC. Effects of pore morphology and bone ingrowth on mechanical properties of microporous titanium as an orthopaedic implant material. *Materials Transactions*. 2004;45(4):1124–1131.
16. Wiley Online Library. Hoboken (NJ): John Wiley & Sons, Inc.; 2014-Jan-20 [Accessed: 2014-Aug-01]. <http://onlinelibrary.wiley.com/store/10.1002/adem.201300431/asset/supinfo/adem201300431-sm-0001-SuppFig-S1.gif?v=1&s=2410042c646030030c12bb1c065d433cecdad07d>.
17. Suryanarayana C. Mechanical alloying and milling. *Progress in Materials Science*. 2001;46(1–2):1–184.
18. Youssef KM, Scattergood RO, Murty KL, Horton JA, Koch CC. Ultrahigh strength and high ductility of bulk nanocrystalline copper. *Applied Physics Letters*. 2005;87(9):091904.
19. Simoes S, Calinas R, Vieira MT, Vieira MF, Ferreira PJ. In situ TEM study of grain growth in nanocrystalline copper thin films. *Nanotechnology*. 2010;21(14):145701.
20. Lu L, Tao NR, Wang LB, Ding BZ, Lu K. Grain growth and strain release in nanocrystalline copper. *Journal of Applied Physics*. 2001;89(11):6408–6414.
21. Atwater MA, Mula S, Scattergood RO, Koch CC. Thermal stability of nanocrystalline copper alloyed with antimony. *Metallurgical and Materials Transactions A*. 2013;44(12):5611–5616.
22. Rajgarhia RK, Saxena A, Spearot DE, Hartwig KT, More KL, Kenik EA, Meyer H. Microstructural stability of copper with antimony dopants at grain boundaries: experiments and molecular dynamics simulations. *Journal of Materials Science*. 2010;45(24):6707–6718.
23. Subramanian PR, Laughlin D. Phase Diagrams of Binary Copper Alloys. Materials Park (OH): ASM International; 1994.
24. Fang TH, Li WL, Tao NR, Lu K. Revealing extraordinary intrinsic tensile plasticity in gradient nano-grained copper. *Science*. 2011;331(6024):1587–1590.

25. Smith CS, Guttman L. Measurement of internal boundaries in 3-dimensional structures by random sectioning. Transactions of the American Institute of Mining and Metallurgical Engineers. 1953;197(1):81–87.
26. VanLeeuwen BK, Darling KA, Koch CC, Scattergood RO. Novel technique for the synthesis of ultra-fine porosity metal foam via the inclusion of condensed argon through cryogenic mechanical alloying. Materials Science and Engineering A. 2011;528(4–5):2192–2195.
27. Davis J. Copper and copper alloys: ASM specialty handbook. Materials Park (OH): ASM International; 2001.
28. Kim JY, Rodriguez JA, Hanson JC, Frenkel AI, Lee PL. Reduction of CuO and Cu₂O with H₂: H embedding and kinetic effects in the formation of suboxides. Journal of the American Chemical Society. 2003;125(35):10684–10692.
29. Rodriguez JA, Kim JY, Hanson JC, Perez M, Frenkel AI. Reduction of CuO in H₂: in situ time-resolved XRD studies. Catalysis Letters. 2003;85(3–4):247–254.
30. Tschopp M, Groeber M, Fahringer R, Simmons J, Rosenberger A, Woodward C. Automated detection and characterization of microstructural features: application to eutectic particles in single crystal Ni-based superalloys. Modelling and Simulation in Materials Science and Engineering. 2010;18(2):025014.
31. Tiley J, Viswanathan G, Shiveley A, Tschopp M, Srinivasan R, Banerjee R, Fraser H. Measurement of γ' precipitates in a nickel-based superalloy using energy-filtered transmission electron microscopy coupled with automated segmenting techniques. Micron. 2010;41(6):641–647.
32. Tschopp M, Groeber M, Fahringer R, Simmons J, Rosenberger A, Woodward C. Symmetry-based automated extraction of microstructural features: application to dendritic cores in single-crystal Ni-based superalloys. Scripta Materialia. 2010;62(6):357–360.
33. Torquato S. Random heterogeneous materials: microstructure and macroscopic properties. New York (NY): Springer; 2002. Vol. 16.
34. Jiao Y, Stillinger F, Torquato S. Modeling heterogeneous materials via two-point correlation functions: basic principles. Physical Review E. 2007;76(3):031110.
35. Jiao Y, Stillinger F, Torquato S. Modeling heterogeneous materials via two-point correlation functions. II. Algorithmic details and applications. Physical Review E. 2008;77(3):031135.

36. Tewari A, Gokhale A, Spowart J, Miracle D. Quantitative characterization of spatial clustering in three-dimensional microstructures using two-point correlation functions. *Acta Materialia*. 2004;52(2):307–319.
37. Gokhale A, Tewari A, Garmestani H. Constraints on microstructural two-point correlation functions. *Scripta Materialia*. 2005;53(8):989–993.
38. Lu B, Torquato S. Lineal-path function for random heterogeneous materials. *Physical Review A*. 1992;45(2):922.
39. Coker DA, Torquato S. Extraction of morphological quantities from a digitized medium. *Journal of Applied Physics*. 1995;77(12):6087–6099.
40. Tschopp MA, Wilks GB, Spowart JE. Multi-scale characterization of orthotropic microstructures. *Modelling and Simulation in Materials Science and Engineering*. 2008;16(6):065009.
41. Wilks GB, Tschopp MA, Spowart JE. Multi-scale characterization of inhomogeneous morphologically textured microstructures. *Materials Science and Engineering A*. 2010;527(4–5):883–889.
42. Tschopp MA, Wilks GB, Spowart JE. Multiscale characterization of spatial heterogeneity in multiphase composite microstructures. *Journal of Engineering Materials and Technology*. 2011;133(1):011004.
43. Li D, Tschopp M, Khaleel M, Sun X. Comparison of reconstructed spatial microstructure images using different statistical descriptors. *Computational Materials Science*. 2012;51(1):437–444.
44. Yeong C, Torquato S. Reconstructing random media. *Physical Review E*. 1998;57(1):495.
45. Fullwood DT, Niezgoda SR, Kalidindi SR. Microstructure reconstructions from 2-point statistics using phase-recovery algorithms. *Acta Materialia*. 2008;56(5):942–948.
46. Atwater MA, Darling KA, Tschopp MA. Towards reaching the theoretical limit of porosity in conventional solid state metal foams: intraparticle expansion as a primary and additive means to create porosity. *Advanced Engineering Materials*. 2014;16:190–195.

Appendix A. MATLAB TPCF Nonperiodic Function

This appendix appears in its original form, without editorial change.

```

function [TPCF] = compute_TPCF_nonperiodic(Z)
% Mark Tschopp, U.S. Army Research Laboratory, 2013-2014
% Email: mark.a.tschopp@us.army.mil
%
% This function computes a two-point correlation function matrix TPCF for
% the non-periodic 2D matrix Z. In the final step, the symmetry due to
% using the FFT functions is reduced. This TPCF is for non-periodic
% systems; periodic systems will need to be handled differently.
%
% Note that the TPCF along a particular direction can be assessed from this
% matrix. For instance, the TPCF along the x direction of matrix Z (size
% 1000 x 1000) is TPCF(1:1000,1) or along the y direction is TPCF(1,1:1000)
% or along 45 degree line is <a = TPCF(1:1000,1:1000); TPCF =
% a(eye(1000)==1);> etc. When plotting TPCF along angles, remember to
% account for the change in the spacing between elements of the matrix,
% i.e., d = d*sqrt(2) for the 45 degree case. For -45 degree case, use the
% bottom half of matrix TPCF, i.e.,
% <a = flipud(TPCF(size(TPCF,1)-1000:size(TPCF,1),1:1000));
% TPCF = a(eye(1000)==1);>.

    f = ifftn(fftn(Z,2*size(Z)).*conj(fftn(Z,2*size(Z))));
    f1 = ifftn(fftn(ones(size(Z)),2*size(Z)).*conj(fftn(ones(size(Z)),...
        2*size(Z))));
    f2 = f./f1;
    TPCF = f2(1:size(f2,1),1:size(Z,2));

end

```

```

function [TPCF] = compute_TPCF_nonperiodic_slow(Z)
% Mark Tschopp, U.S. Army Research Laboratory, 2013-2014
% Email: mark.a.tschopp@us.army.mil
%
% This function computes a two-point correlation function matrix TPCF for
% the non-periodic 2D matrix Z in direction X (dimension 1 of matrix Z).
% This TPCF is for non-periodic systems; periodic systems will need to be
% handled differently.
%
% Note that the TPCF along this direction is assessed for each row in the
% matrix Z. For instance, TPCF(1,:) gives the TPCF for row 1 of matrix Z,
% TPCF(2,:) gives the TPCF for row 2 of matrix Z. The 'mean' operation can
% be used to give the global TPCF for the 2D matrix Z in this direction.
%
% The TPCF in direction Y (dimension 2 of Z) can be computed using:
% [TPCF] = compute_TPCF_nonperiodic_slow(transpose(Z))

TPCF = zeros(size(Z));
for i=1:size(Z,1)
    a = Z(i,:);
    b = find(a == 1);
    n = length(b(b <= length(Z)));
    for j = 1:n-1
        c = b - b(1);
        c = c(2:end);
        d = c(c <= length(Z));
        TPCF(i,d) = TPCF(i,d) + 1;
        b = c;
    end
end

% Divide by the total number in each row
for i = 1:size(Z,2)-1
    TPCF(:,i) = TPCF(:,i)/(size(Z,2)-i);
end

end

```

INTENTIONALLY LEFT BLANK.

Appendix B. MATLAB TPCF Periodic Function

This appendix appears in its original form, without editorial change.

```

function [TPCF] = compute_TPCF_periodic(Z)
% Mark Tschopp, U.S. Army Research Laboratory, 2013-2014
% Email: mark.a.tschopp@us.army.mil
%
% This function computes a two-point correlation function matrix TPCF for
% the periodic 2D matrix Z. Because of the periodic boundary, this TPCF
% matrix is half of the size of the original 2D matrix Z. This TPCF is for
% periodic systems only; non-periodic systems will need to be handled
% differently.
%
% Note that the TPCF along a particular direction can be assessed from this
% matrix. For instance, the TPCF along the x direction of matrix Z (size
% 1000 x 1000) is TPCF(1:500,1) or along the y direction is TPCF(1,1:500)
% or along 45 degree line is TPCF(eye(500)==1), etc. When plotting TPCF
% along angles, remember to account for the change in the spacing between
% elements of the matrix, i.e.,  $d = d \cdot \sqrt{2}$  for the 45 degree case. For
% -45 degree case, use the bottom half of matrix TPCF, i.e.,  $\langle a =$ 
% TPCF(flipud(eye(500))==1)>.

    f = ifftn(fftn(Z).*conj(fftn(Z)));
    f = f(1:size(f,1)/2,1:size(f,2)/2);
    TPCF = f/numel(Z);

% If you want to expand to the same size as Z, use:
% TPCF = (ifftn(fftn(Z).*conj(fftn(Z))))/numel(Z);
% or use symmetry to expand... (because the TPCF at d=100 is the same as
% d=300 for a 400x400 matrix Z)

end

```

Appendix C. MATLAB LPF Nonperiodic Function

This appendix appears in its original form, without editorial change.

```

function [LPF] = compute_LPF_2D_nonperiodic(Z)
% Mark Tschopp, U.S. Army Research Laboratory, 2013-2014
% Email: mark.a.tschopp@us.army.mil
%
% This function computes a lineal path function matrix TPCF for the
% non-periodic 2D matrix Z in direction X (dimension 1 of matrix Z). This
% LPF is for non-periodic systems; periodic systems will need to be handled
% differently.
%
% Note that the LPF along this direction is assessed for each row in the
% matrix Z. For instance, LPF(1,:) gives the LPF for row 1 of matrix Z,
% LPF(2,:) gives the LPF for row 2 of matrix Z. The 'mean' operation can
% be used to give the global LPF for the 2D matrix Z in that direction.
%
% The LPF in direction Y (dimension 2 of Z) can be computed using:
% [LPF] = compute_LPF_2D_nonperiodic(transpose(I))
%
% The LPF for a different phase can be computed using
% [LPF] = compute_LPF_2D_nonperiodic(~I)
% for 2 phases (in a logical matrix), OR
% [LPF] = compute_LPF_2D_nonperiodic(I==n)
% for multiple phases

% LPF of phase Z==1
LPF = zeros(size(Z));
for i = 1:size(Z,1)
    a = Z(i,:);
    b = find(a == 1);
    while length(b) > 1
        c = diff(b);
        d = find(c~=1);
        if isempty(d)==0 && d(1)~=1;
            e = b(2:d(1))-b(1);
            f = sort(e, 'descend');
            LPF(i,e) = LPF(i,e) + f(e);
            b = b(d(1)+1:end);
        elseif isempty(d)==1;
            e = b(2:end)-b(1);
            f = sort(e, 'descend');
            LPF(i,e) = LPF(i,e) + f(e);
            b = 1;
        elseif d(1)==1;
            b = b(d(1)+1:end);
        end
    end
end

```



```

        end
    end
end

% Divide by the total number in each row
for i = 1:size(Z,2)-1
    LPF(:,i) = LPF(:,i)/(size(Z,2)-i);
end

```

INTENTIONALLY LEFT BLANK.

List of Symbols, Abbreviations, and Acronyms

2-D	2-dimensional
3-D	3-dimensional
EBS	electron backscatter diffraction
FFT	fast Fourier transform
FIB	focused ion beam
FIBCCI	focused ion beam channeling contrast imaging
LPF	lineal path function
SEM	scanning electron microscopy
TPCF	2-point correlation function

1 DEFENSE TECHNICAL
(PDF) INFORMATION CTR
DTIC OCA

2 DIRECTOR
(PDF) US ARMY RESEARCH LAB
RDRL CIO LL
IMAL HRA MAIL & RECORDS MGMT

1 GOVT PRINTG OFC
(PDF) A MALHOTRA

35 RDRL WM
(PDF) B FORCH
S KARNA
J MCCAULEY
RDRL WMM
J BEATTY
R DOWDING
J ZABINSKI
RDRL WMM A
M GRIEP
L HOLMES
J SANDS
R RODRIGUEZ
RDRL WMM D
B BARNETT
R BRENNAN
R CARTER
K CHO
A GIRI
B MCWILLIAMS
M PEPI
RDRL WMM E
J ADAMS
J LASALVIA
D SHREIBER
J SINGH
J SWAB
RDRL WMM F
B BUTLER
J CHINELLA
K DARLING
K DOHERTY
S GREND AHL
L KECSKES
E K LIER
H MAUPIN
H MURDOCH
T SANO
M TSCHOPP
RDRL WMM G
J ANDZELM
A RAWLETT